

Quantitative simulation of selective laser melting of metals enabled by new high-fidelity multiphase, multiphysics computational tool

Tao Yu^a, Jidong Zhao^{a,b,*}

^a Hong Kong University of Science and Technology, Clearwater Bay, Kowloon, Hong Kong

^b HKUST Shenzhen-Hong Kong Collaborative Innovation Research Institute, Futian, Shenzhen, China

Received 28 January 2022; received in revised form 20 June 2022; accepted 15 July 2022

Available online xxxx

Abstract

Laser powder bed fusion represents the future for metal additive manufacturing. Advance of this emerging technology is bottlenecked by the unavailability of high-fidelity prediction tools for cost-effective optimization on printing design. Simulations of selective laser melting of metals must tackle a complex granular solids and multiphase fluids system that undergoes intra- and inter-phase interactions and thermal-induced phase changes, including melting, vaporization, and solidification, which are challenging to model. We develop a high-fidelity computational tool to provide high-resolution simulations of the multiphase, multiphysics processes of selective laser melting (SLM). Key to this tool is a multi-phase, semi-coupled resolved Computational Fluid Dynamics (CFD) and Discrete Element Method (DEM). It contains innovative features including (1) a fully resolved immersed boundary CFD with fictitious particle domain coupling with DEM for resolving mechanical interactions and heat transfers between solid particles and surrounding fluid; (2) An evaporation model in consideration of the Knudsen layer implemented in the volume of fluid (VOF) method which is enriched by two sharp interface capture schemes, isoAdvector and MULES, for accurate identification of the vaporization process and phase boundaries of fluids with different Courant numbers; and (3) a ray tracing model compatible with the VOF method for high-resolution of absorbed laser energy. We demonstrate the proposed method can quantitatively reproduce key observations from synchrotron experiments and captures critical interdependent physics involving melt pool morphology evolution, vapor-driven keyhole dynamics and powder motions. This new computational tool opens a new avenue for quantitative design and systematic optimization of laser powder bed fusion and may find wider engineering applications where thermal induced phase changes in a multi-phase system are important.

© 2022 Elsevier B.V. All rights reserved.

Keywords: Granular powder; Coupled CFD-DEM; Multiphase fluids; Selective laser melting; Additive manufacturing

1. Introduction

Selective laser melting (SLM) of metallic powders represents one prevailing technology of laser powder bed fusion (LPBF) for additive manufacturing. It uses laser beams to melt metallic powders layer by layer to print complex parts without constraints by design in conventional manufacturing industries [1–4]. SLM commonly utilizes high-power laser to melt single-material metallic powders to build parts with ultra-high mechanical properties. It

* Corresponding author at: Hong Kong University of Science and Technology, Clearwater Bay, Kowloon, Hong Kong.
E-mail address: jzhao@ust.hk (J. Zhao).

is featured by multiple types of phase changes during the melting process, including melting, vaporization, and solidification [5,6]. Indeed, the SLM process is frequently dominated by the vaporization of melt liquid in the melt pool due to absorption of laser power, generating high-speed vapors that circulate and escape from the melt pool and entrain surrounding ambient gas and powders to interact with the melt pool dynamics [5].

The future developments of the SLM technology hinge crucially upon overcoming an array of challenges to reduce detrimental defects in the final printed parts including poor surface roughness [7] and high porosity [8]. The formation of these defects is governed by complicated interactions among high-speed vapor, vapor-induced powder motions and melt pool dynamics in SLM [5,9–11]. Understanding the underlying physics of these processes proves to be pivotal for accurate characterization of all other aspects of SLM, whereas capturing these key physical phenomena and understanding their mechanisms often demand advanced observational technologies which are currently unavailable [8,12–14]. Numerical approaches appear to be the only viable, cost-effective pathway to tackling the challenges [15]. Specifically, the fusion and vaporization of metallic powders in SLM pose a common complicated multiphase, multiphysics problem featured by both intra-phase and inter-phase thermal transfers, thermal-induced phase transformations, and kinetic and mechanical interactions among solid grains, melt liquid, high-speed metallic vapor, and ambient gas during the entire melting process. It is desirable to develop a rigorous simulation framework that can integrate such a complex dynamical multiphase system with rigorous consideration of the underlying multi-physics processes in SLM.

Collective efforts [16–48] have been made toward developing advanced numerical approaches to reproduce experimentally observed features [8,49,50] manifested in the thermal-induced phase transformation processes to analyze the porosity formation and powder–liquid–vapor interactions [12,51–53]. It remains a challenge, however, to rigorously model in SLM the vaporization process and the induced high-speed vapor and the causation of ambient gas turbulence and powder motions, and hence their interwound interactions with the melt pool dynamics in a realistic 3D setting.

We propose herein a rigorous, physically based computational framework to tackle these challenges in SLM for next-generation simulation of metallic powder based additive manufacturing. The new numerical framework is built upon the success of our previous coupled computational fluid dynamics and discrete element method (CFD-DEM) modeling of granular systems [53], with the following major innovative considerations that revolutionize its predictive capabilities. (1) A multi-phase fully resolved CFD formulation is coupled with the DEM to enable the simulation of more realistic four-way interactions among the three-phase fluids (melt liquid, vapor, and gas) and the solid powder particles. (2) A novel evaporation model accounting for the Knudsen layer is implemented in the volume of fluid (VOF) method for accurate simulation of the vaporization process where the VOF method is further extended to solve the volume fraction field in CFD in conjunction with two sharp interface capture schemes, isoAdvector and MULES, for the corresponding fluids according to their Courant number. (3) To enable high-fidelity simulation of laser-induced vaporization and vapor motion, a new ray tracing laser model compatible with the VOF method is proposed for accurate calculation of absorbed laser energy.

As will be demonstrated, the newly proposed multi-phase, semi-coupled resolved CFD-DEM framework, featured by solving the dynamics of a multi-phase fluid-particle system with fully resolved CFD-DEM and the thermal field of multi-phase fluid-particle system with multi-phase CFD, enables us to make high-fidelity, high-resolution predictions on key phenomena observed in advanced experiments based on rigorous consideration of key interdependent physics, including multi-way phase changes such as melting, vaporization and solidification wherein the Fresnel reflection and refraction [54], laser penetration and absorption [55], recoil pressure [8], vapor pressure [56], Marangoni's flow [8], and Darcy's effect [57,58]. It also enables quantitative analyses of the influence of laser power and scanning velocity on the melt pool morphology, melt pool evolution and powder motions in SLM for printing optimization. The SLM case will be spotlighted with detailed analysis due to the rich physics involved in the process, providing a better demonstration of the predictive capability of our proposed approach.

2. Methodology: Multi-phase semi-coupled resolved CFD-DEM

2.1. Consideration of a multiphase system involving powders, melt liquid, vapor and ambient gas

We herein employ the volume of fluid (VOF) method in conjunction with two sharp interface capture schemes, MULES and isoAdvector [59], coupled further with DEM to furnish such an integrated computational framework for modeling of such a multiphase system involving in SLM. We consider a body of solid granular grains in a fluid

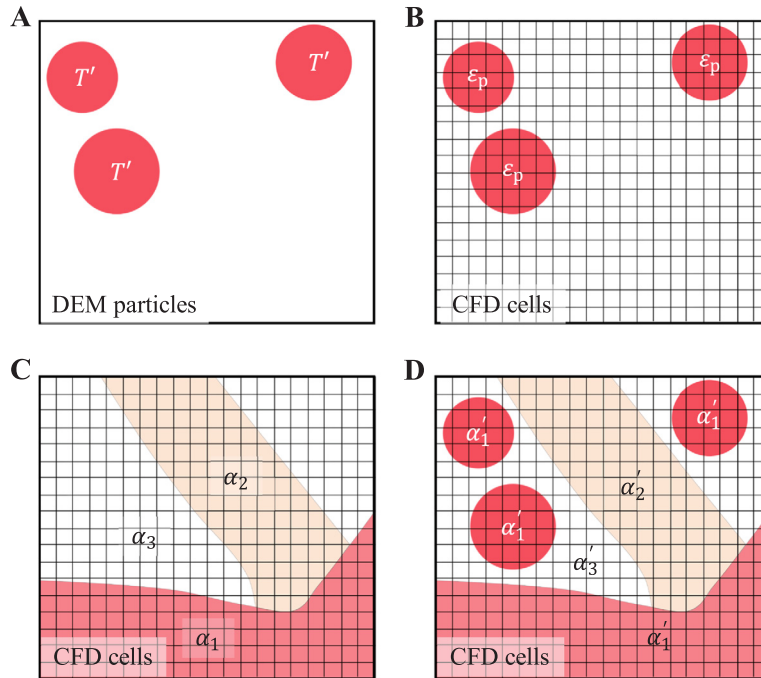


Fig. 1. Schematic illustration of the multiphase system consisting of solid powders, melt liquid, vapor and ambient gas to be treated by semi-coupled fully resolved CFD-DEM. (A) Solid granular particles with tagged temperature T' simulated by DEM. (B) Fictitious CFD cells in a CFD domain that occupy the physical space of DEM particles represented by a void fraction ε_p . (C) Original CFD domain for a multi-phase fluid system comprised melt flow, vapor flow and ambient gas in SLM, represented respectively by their volume fraction $\alpha_i (i = 1, 3)$. (D) Aggregated CFD domain integrating original and fictitious CFD domains for solid particles in (B) and the multiphase fluid system in (C). Note that the subscript i represents the material type and α'_i in (D) denotes the overall volume fraction in consideration of both DEM particles and CFD fluids. $\alpha'_1 = \alpha_1 + 1 - \varepsilon_p$, considering the static and moving DEM particles and CFD melt particles. The integrated CFD domain in (D) will be applied for solving the thermal field in the multi-phase semi-coupled resolved CFD-DEM approach. Note that the above illustration has been in 2D for the convenience of explanation and all subsequent simulations have been performed in full 3D.

domain of multiphase flows for a typical setting of SLM. Fig. 1 shows how the coupled CFD-DEM approach is employed to treat such a complex system.

The CFD with the VOF scheme is used to treat the fluid domain consisting of co-existing multiphase flows including molten or partially melted solid grains, metallic vapor, and ambient gas (Fig. 1C). To overcome the limitation of VOF which can only obtain a smeared interface between different phases, two sharp interface capture schemes, MULES and isoAdvector [59], are employed in this study to describe different fluid phases according to the Courant number to achieve a balance between the computational cost and efficiency. As a default scheme in *OpenFOAM* [60], the CFD code to be used here, MULES treats the smeared interface by adding a compressive flux term $\nabla \cdot (\alpha_i(1 - \alpha_i)\mathbf{u}_c)$ into the LHS of the advection equation of phase i [61] such that the Courant number can be larger than 1 with the implicit MULES scheme. $\mathbf{u}_c = (c |\mathbf{u}_f| \nabla \alpha_i) / |\nabla \alpha_i|$ is the compressed velocity, \mathbf{u}_f is the fluid velocity, α_i is the volume fraction of phase i and $c \in (0, 1)$ is the coefficient to control the compressed velocity. The isoAdvector scheme has been proved to offer a better resolved interface than the MULES scheme [60,62], whereas an accurate prediction requires the mesh size and time step to be limited to $CFL < 1$ [63]. In this scheme, the cell volume fraction is first interpolated to vertices, and isosurfaces in the cells containing the interface are reconstructed to calculate accurate surface flux based on the volume fractions of eight vertices. The volume fraction field for the next time step can then be obtained using the integral of the surface flux, with further application of a bounding procedure to avoid the values of volume fraction from being out of range, leading to the final interface [59]. In this study, the implicit MULES scheme is employed for the simulation of high-speed vapor with varied speeds ranging from tens of meters per second to hundreds of meters per second depending on the laser power [5,6]. Partially melted powders and the melt flow are solved by the isoAdvector scheme, since the complicated surface

morphology featured with ripples, pores, denudation and balling effect in SLM demands an accurate interface, and meanwhile the relatively low velocity of these phases helps to satisfy the required CFL condition.

In simulating the thermal field for a solid grain, the DEM is typically limited to a representation of single temperature field of an entire particle rather than presenting an actual temperature gradient within the individual solid particle, unless we resort to using exceedingly complicated and costly numerical treatments (e.g., by refining each particle to small elements [64]). To avoid the potential complications for DEM, a multi-phase CFD is employed by considering a fictitious CFD domain that occupies the actual physical space of a DEM particle (Fig. 1B). This technique helps to overcome the aforementioned limitation in DEM modeling and offer a high-resolution thermal field solution that accounts for realistic partial or progressive melting of a solid grain due to the presence of temperature gradient during the melting process.

Specifically, as shown in Fig. 1(A and B), the void fraction and the tagged temperature of DEM particles in a fluid cell are denoted as ε_p and T' , respectively. In the multi-phase CFD consideration of the fictitious domain of DEM particles (Fig. 1B), the void fraction ε_p can be determined by $\frac{1}{8} \sum_{i=1}^8 k_v$, where $k_v = 0$ when the i th vertex of the cubic cell is within the DEM particle, i.e., the distance between the vertex and the particle center is smaller than the particle radius, and $k_v = 1$ when the i th vertex of the cubic cell is outside the DEM particle. $0 < \varepsilon_p < 1$ is indicative of an interface cell, with the bounding values of 0 and 1 denoting respectively to a cell located entirely inside or outside of the DEM particle. In a multiphase CFD domain (Fig. 1C), the volume fractions of three fluid phases, i.e., the melt flow, the metallic vapor, and the ambient gas in a general setting of SLM, are denoted as α_1 , α_2 , and α_3 , respectively, and $\sum_i \alpha_i = 1$. The VOF method is intended to solve a region containing interface cells with a volume fraction ranging from 0 to 1, as shown in Fig. 2B, similar to the void fraction ε_p . The overall volume fraction α'_i (Fig. 1D) comprising the fictitious CFD domain and the original CFD domain is constructed for the thermal field calculation. The overall volume fraction of metal ($\alpha'_1 = \alpha_1 + 1 - \varepsilon_p$) will be used in the subsequent ray tracing model to consider the static and moving DEM particles and CFD fluids. Based on the above consideration in the multi-phase semi-coupled fully resolved CFD-DEM, we are ready to obtain the corresponding equivalent density ρ and viscosity μ in the momentum equation and the revised expressions considering the fictitious CFD domain occupied by the actual positions of the DEM particle for the density ρ_T , dynamic viscosity μ_T , thermal conductivity k , and heat capacity C in the energy equation over the entire domain.

The equivalent density ρ and viscosity μ in the momentum equation and the revised expressions considering the fictitious CFD domain occupied by the actual positions of the DEM particle for the density ρ_T , dynamic viscosity μ_T , thermal conductivity k , and heat capacity C in the energy equation over the entire domain could be written as:

$$\left\{ \begin{array}{l} \rho = \sum \alpha_i \rho_i \\ \mu = \sum \alpha_i \mu_i \\ \rho_T = \varepsilon_p \sum_i \alpha_i \rho_i + (1 - \varepsilon_p) \rho_p \\ \mu_T = \varepsilon_p \sum_i \alpha_i \mu_i + (1 - \varepsilon_p) \mu_p \\ k = \varepsilon_p \sum_i \alpha_i k_i + (1 - \varepsilon_p) k_p \\ C = \varepsilon_p \sum_i \alpha_i \frac{\rho_i}{\rho_T} C_i + (1 - \varepsilon_p) \frac{\rho_p}{\rho_T} C_p, \end{array} \right. \quad (1)$$

where ε_p is the void fraction of DEM particles, α_i ($i = 1, 3$) is the volume fraction of i th phase of fluids (e.g., melt liquid, metal vapor, and ambient gas). ρ_i , μ_i , k_i and C_i are the density, viscosity, heat conductivity, and heat capacity of i th phase of fluid, respectively. ρ_p , k_p , and C_p are the density, heat conductivity, and heat capacity of the particle, respectively.

2.2. Treatment of inter-phase boundaries by a VOF compatible evaporation model

In the SLM simulation, accurate descriptions of the boundary and the ensuing interactions between the melt flow and high-speed metallic vapor is critically important for faithful reproduction of the melt pool dynamics. We

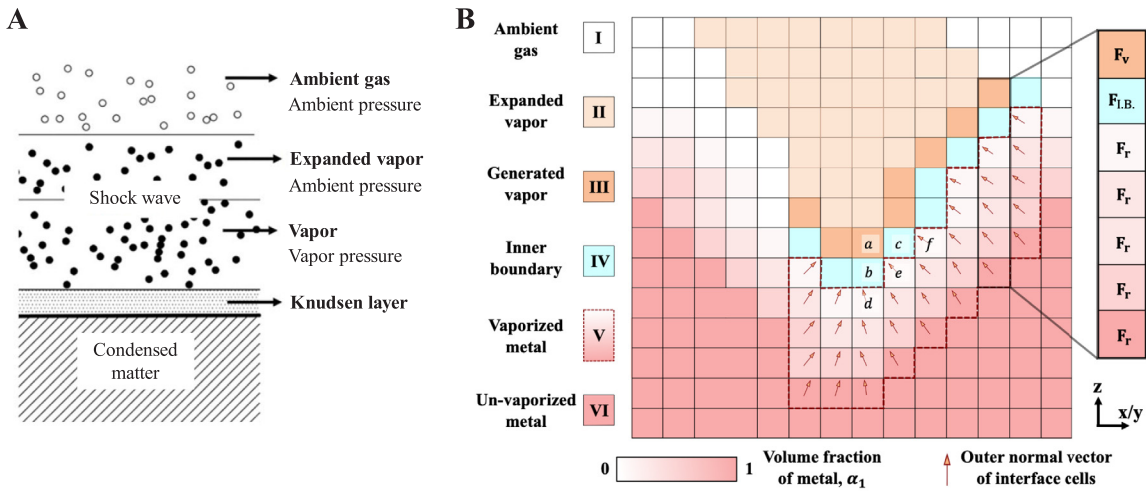


Fig. 2. (A) Physical structure of classic evaporation model in a common atmosphere [65]. (B) 2D Schematic diagram for the proposed VOF compatible evaporation model. Regions I to VI represent the ambient gas, the expanded vapor, the generated vapor, the inner boundary, the vaporized metal, and the un-vaporized metal, respectively. Region V represents the metal with a temperature exceeding the boiling temperature. The Knudsen layer is a thin layer of vapor near the vaporized metal in SLM, separating the vaporized metal and external continuum vapor, and the equivalent inner boundary (Region IV) with a pressure drop $F_{L.B.}$ plays the same role in separating the generated vapor (Region III) driven by the vapor pressure F_v and the vaporized metal (Region V) driven by the recoil pressure F_r . The volume fraction of Region II ranging from 0 to 1 is solved by the VOF method and dominated by the vapor mass ratio of Region III. The arrows in (B) are the outer normal vectors of the interface cells. Cells *a*, *b*, *c*, and *e* construct a basic evaporation unit in the evaporation model.

herein propose a VOF compatible evaporation model to rigorously simulate the evolving interface behavior at the inter-phase boundaries during SLM. The construction of such a model makes specific reference to a classic physical model in common atmosphere to define the equivalent interface structure and to differentiate different layers, as explained in the following.

Classic evaporation model: Fig. 2A shows the physical structure of a classic evaporation model in common atmosphere [65]. Five typical layers are commonly considered in a classic evaporation model, namely, the condensed matter, the Knudsen layer, the generated vapor, the expanded vapor and the ambient gas. The Knudsen layer refers to a thin layer of vapor [66] between the condensed matter and the external continuum vapor flow. Its thickness may amount to several mean free path of gas molecules [67] (e.g., around 2 μm for the vapor of Ti-6Al-4V). The Knudsen layer serves as a kinetic boundary layer moving with the surface of the condensed matter and can be simplified as a discontinuity [65]. In practice, it works as an inner boundary to separate the condensed matter driven by the recoil pressure and the external continuum vapor flow driven by the vapor pressure.

Equivalent interface structure: With reference to Fig. 2A, an equivalent interface model is constructed in this study to match the physical structure with the computational partitions, as shown in Fig. 2B. To account for the Knudsen layer, an equivalent inner boundary is constructed for the multiphase model where a size of the mesh resolution (4 ~ 5 μm) is adopted for the boundary thickness on balance of computational efficiency and accuracy. The inner boundary (Region IV) is near the surface of vaporized metal (Region V) over which the vapor is generated from the cells (Region III). Note that the metal surface solved by the VOF method is a region of interface cells containing a mixture of two phases (e.g., metal and ambient gas) with a volume fraction ranging from 0 to 1, such that the inner boundary should be constructed above the whole interface region (Region V) along the normal vector direction. Consequently, six equivalent layers (Regions I to VI in Fig. 2B) comparable to the classic evaporation model are constructed in our numerical model, including the ambient gas, the expanded vapor, the generated vapor, the inner boundary, the vaporized metal and the un-vaporized metal. The vaporized metal remains in metal fluid state yet with a temperature higher than the boiling temperature to allow evaporation to occur.

Region identification: In each time step, Region III needs further to be differentiated from Region IV according to the vaporized metal cells identified for Region V. Region V is first identified wherein the vaporized metal cells are found to a metal volume fraction $\alpha_1 > 0$ and a temperature $T > T_{LV}$ (where T_{LV} is the boiling temperature). Since the inner boundary (Region IV) is near the surface of the vaporized metal cells (Region V), Cell *j* in the

inner boundary with a metal volume fraction $\alpha_1 = 0$ is identified if it is adjacent to Cell i in Region V. Cell j satisfies $|\mathbf{C}_i - \mathbf{C}_j| = \Delta L$, where ΔL is the mesh size and \mathbf{C}_i and \mathbf{C}_j are the cell center vectors of Cell i and Cell j , respectively. Likewise, the generated vapor cell k in Region III with a metal volume fraction $\alpha_1 = 0$ is adjacent to the inner boundary cell j , satisfying $|\mathbf{C}_j - \mathbf{C}_k| = \Delta L$.

Transformation of vaporized metal to vapor: The mass, pressure and energy terms for the generated vapor cells in Region III are calculated based on the mass loss ratio, recoil force and temperature field of vaporized metal cells in Region V. Since the recoil force is perpendicular to the surface of vaporized metal, the mass loss ratio $(\dot{m}_r)_i$, recoil force $(\mathbf{F}_r)_i$ and temperature T_i of the vaporized metal cell i only contribute to the generated vapor cell k along the normal of Cell i to satisfy the conservation of mass, momentum, and energy. It is readily evident that the vapor mass ratio \dot{m}_v , vapor pressure \mathbf{F}_v and the energy correction term ϕ_v applied on the generated vapor cell k can be respectively calculated by Eqs. (2) to (4). In the current model, if the distance from Cell k to the normal of Cell i with a normal vector $\mathbf{n}_i = (\nabla\alpha_1/|\nabla\alpha_1|)_i$ is smaller than the half of mesh size ΔL , it is assumed that the generated vapor cell k is along the normal of Cell i .

$$(\dot{m}_v)_k = - \sum_i (\dot{m}_r)_i, \tag{2}$$

$$(\mathbf{F}_v)_k = - \sum_i (\mathbf{F}_r)_i, \tag{3}$$

$$(\phi_v)_k = \sum_i C_{1i} (|\dot{m}_r|)_i (T_i - T_k), \tag{4}$$

where i represents the vaporized metal Cell i in region V satisfying the distance $d_{vik} = \sqrt{(\mathbf{C}_i - \mathbf{C}_k) \cdot (\mathbf{C}_i - \mathbf{C}_k) - (\mathbf{n}_i \cdot (\mathbf{C}_i - \mathbf{C}_k))^2}$ from Cell k to the normal of Cell i is smaller than $\Delta L/2$ and the distance $d_{ik} = |\mathbf{C}_i - \mathbf{C}_k|$ between Cell i and Cell k is also the minimum compared with the distance from other cells in Region III to Cell i .

Basic evaporation unit: A basic evaporation unit is further constructed for the evaporation model to include the vaporized metal cell at the top surface of Region V and its adjacent inner boundary cells in Region IV and the generated vapor cell in Region III along the normal of the vaporized metal cell. Take an example in Fig. 2B, Cell a in Region III, Cell d in Region V and Cells b and c in Region IV are joined to construct a basic evaporation unit. We can set the vaporized metal cell as the reference frame for each basic evaporation unit. The relative velocity of the inner boundary cells should be set to 0 as the inner boundary is always adjacent to the vaporized metal surface. The relative velocity of the generated vapor cell is dominated by the vapor pressure. It works similarly to the partially melting region that separates the static solidified part and the fully melt free flowing part.

Pressure drop of inner boundary: A pressure drop applied on the inner boundary is constructed to separate the vaporized metal and the generated vapor as two discrete phases. The pressure drop $\mathbf{F}_{I.B.}$ is similar to the pressure term obtained from the Darcy's effects [68] in Eq. (20) when solving the dynamics of the partially melting region. The pressure drop and density of the inner boundary can be written as

$$\mathbf{F}_{I.B.} = -K_{I.B.} (\mathbf{u}_f - \bar{\mathbf{u}}_t), \tag{5}$$

$$\rho_{I.B.} = \bar{\rho}_t/2, \tag{6}$$

where $K_{I.B.}$ is a coefficient analogous to the permeability coefficient in the Darcy's law. $K_{I.B.}$ equals the permeability coefficient K_c of Darcy's term (see Table 1) in this study for simplicity as the further increase of $K_{I.B.}$ still leads to the same behavior for the inner boundary cells, i.e., $\mathbf{u}_f = \bar{\mathbf{u}}_t$ for the inner boundary cells. \mathbf{u}_f is the velocity of the inner boundary cell, and $\bar{\mathbf{u}}_t$ and $\bar{\rho}_t$ are the mean velocity and mean density of the reference frames of basic evaporation units that the cell under consideration belongs to, respectively. The density of the inner boundary $\rho_{I.B.}$ implies a linear transition between Region III and Region V. Take an example in Fig. 2B, the mean velocity $\bar{\mathbf{u}}_{tb}$ of Cell b is $(\mathbf{u}_{fd} + \mathbf{u}_{fe})/2$ in the 2D case and \mathbf{u}_{fd} and \mathbf{u}_{fe} are the velocities of Cell d and Cell e , respectively. The mean density $\bar{\rho}_{tb}$ of Cell b is $(\rho_{fd} + \rho_{fe})/2$ in the 2D case and ρ_{fd} and ρ_{fe} are the densities of Cell d and Cell e , respectively.

The following summarizes the construction process for the proposed evaporation model.

- (1) Identify the vaporized metal cells (Region V) with $T > T_{LV}$ and $\alpha_1 > 0$, where T_{LV} is the boiling temperature, and calculate the corresponding mass loss ratio \dot{m}_r and recoil pressure \mathbf{F}_r for all vaporized metal cells. Cell

Table 1
Physical parameters of Ti-6Al-4V [53].

Parameter	Value and units	Parameter	Value and units
Molar mass	$M = 446.07 \text{ g/mol}$	Solidus temperature	$T_s = 1878 \text{ K}$
Initial temperature	$T_0 = 300 \text{ K}$	Liquidus temperature	$T_l = 1923 \text{ K}$
Boiling temperature	$T_{LV} = 3133 \text{ K}$	Viscosity of liquid Ti-6Al-4V alloy	$\mu_l = 0.005 \text{ Pa s}$
Latent heat of fusion	$L_f = 2.88 \times 10^5 \text{ m}^2/\text{s}^2$	Convective heat transfer coefficient	$h = 19 \text{ kg s}^3 \text{ K}$
Latent heat of evaporation	$L_V = 4.7 \times 10^6 \text{ m}^2/\text{s}^2$	Change rate of surface tension coefficient	$\frac{\partial \sigma}{\partial T} = -2.6 \times 10^{-4} \text{ kg}/(\text{s}^2 \text{ K})$
Permeability coefficient	$K_c = 5.56 \times 10^6 \text{ kg}/(\text{m}^3 \text{ s})$	Surface tension coefficient at melt point	$\sigma_l = 1.5 \text{ kg}/\text{s}^2$
Refractive index	$e = 3.47$ [52]	Coefficient related to the electrical conductance	$\varepsilon = 0.2$ [51]
Attenuation coefficient	$\gamma = 0.192 \text{ }\mu\text{m}^{-1}$ [20,53,69,70]	Constant to avoid division by zero	$C_K = 10^{-5}$

j with $\alpha_{1j} = 0$ is set as an inner boundary cell (Region IV) if it is adjacent to the vaporized metal Cell i , i.e., $|\mathbf{C}_i - \mathbf{C}_j| = \Delta L$, where ΔL is the mesh size and \mathbf{C}_i and \mathbf{C}_j are the cell center vectors of Cell i and Cell j , respectively. The pressure drop and density of the inner boundary Cell j are calculated by Eqs. (5) and (6), respectively.

- (2) Identify the cells for the generated vapor (Region III) based on the obtained Regions IV and V from Step (1). Cell k with $\alpha_{1k} = 0$ is set as the generated vapor cell if it does not belong to Regions IV and V and is adjacent to inner boundary Cell j , i.e., $|\mathbf{C}_j - \mathbf{C}_k| = \Delta L$. The vapor mass ratio \dot{m}_v , vapor pressure \mathbf{F}_v and energy correction term ϕ_v applied on the generated vapor Cell k are respectively calculated by Eqs. (2) to (4).

2.3. VOF compatible ray tracing model for the laser beam

We further propose a ray tracing model adapted for the VOF method as illustrated in Fig. 3 to accurately consider the Fresnel reflection and refraction for the incident laser and laser energy absorption during the scanning process. The overall volume fraction of the metal α'_1 is used in the ray tracing model to account for the substrate, moving particles, static particles, and melt particles, as explained in Section 2.1 and Fig. 1. The unit normal vector of the interface cells at the metal–gas interface is calculated by Eq. (7). The incident angle θ_l between the incident ray with a unit vector \mathbf{v}_l and the unit normal vector \mathbf{n}_i of the interface Cell i at the interface can be obtained, i.e., $\theta_{li} = \arccos(|\mathbf{n}_i \cdot \mathbf{v}_l|)$, where the initial \mathbf{v}_l is $(0, 0, -1)$ due to the vertical laser beam in z direction. Refer to Fig. 3A and assume the incident angle θ_l equals the reflected angle θ_R and the refracted angle θ_T satisfies $n_l \sin \theta_l = n_T \sin \theta_T$, where n_l and n_T are the refractive indices for two media, respectively. The unit vector of the reflected ray \mathbf{v}_R and the refracted ray \mathbf{v}_T can be respectively obtained by Eqs. (8) to (10).

$$\mathbf{n} = \nabla \alpha'_1 / |\nabla \alpha'_1|, \tag{7}$$

$$\mathbf{v}_R = \mathbf{v}_l - 2(\mathbf{v}_l \cdot \mathbf{n})\mathbf{n}, \tag{8}$$

$$\tilde{\mathbf{v}}_T = \mathbf{v}_l/e - \mathbf{n} \left(\cos \theta_l/e - \sqrt{1 - (1 - \cos \theta_l \cdot \cos \theta_l)/e^2} \right), \tag{9}$$

$$\mathbf{v}_T = \tilde{\mathbf{v}}_T / |\tilde{\mathbf{v}}_T|, \tag{10}$$

$$d_{R(T)ij} = \sqrt{(\mathbf{C}_i - \mathbf{C}_j) \cdot (\mathbf{C}_i - \mathbf{C}_j) - (\mathbf{v}_{R(T)i} \cdot (\mathbf{C}_i - \mathbf{C}_j))^2}, \tag{11}$$

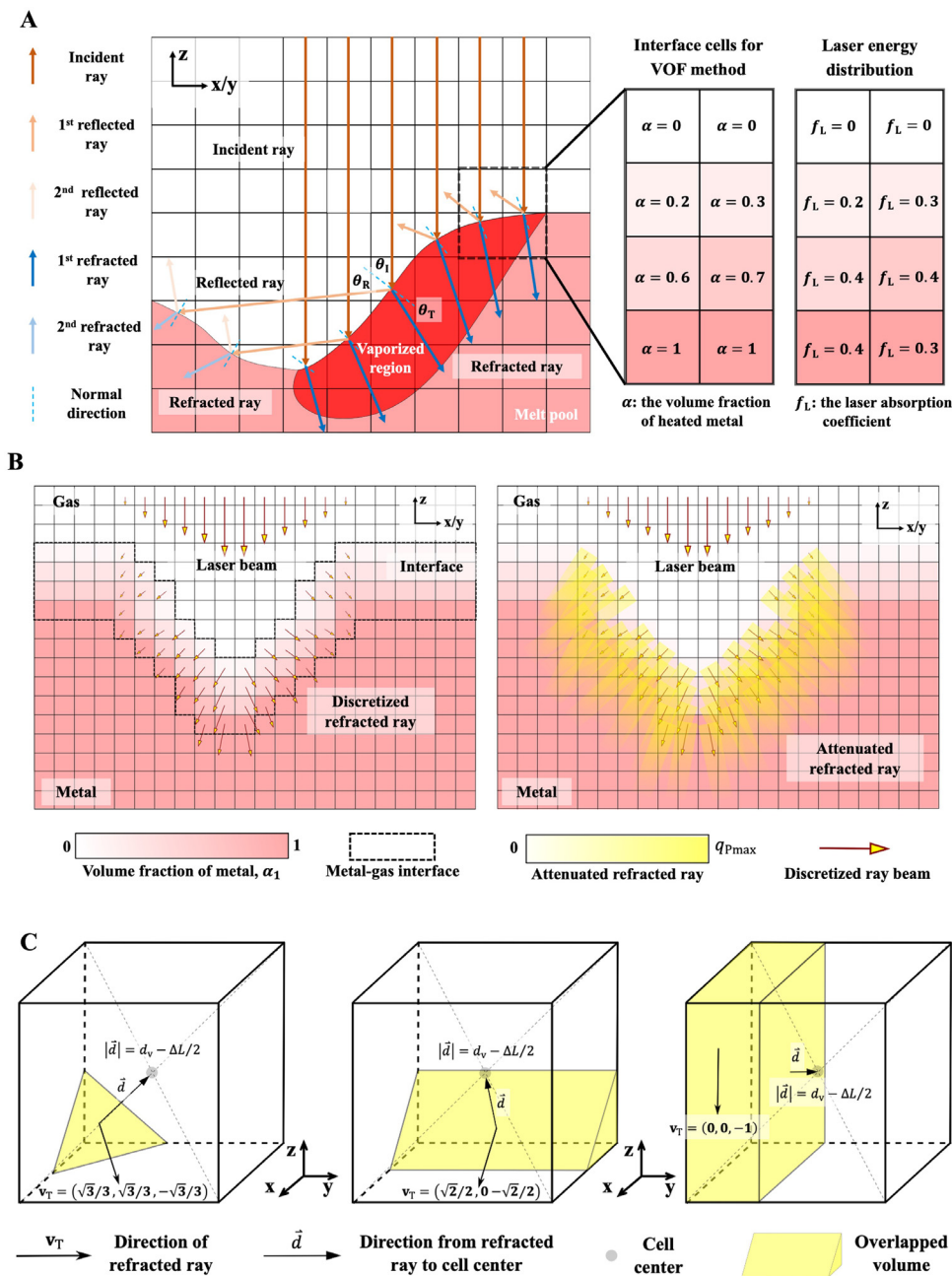


Fig. 3. Schematic diagram for the VOF compatible ray tracing model. (A) 2D illustration of the ray tracing model. Left: Fresnel reflection and refraction. Right: an example of interface cells obtained by the VOF method and energy distribution of laser discretization on the interface cells. (B) 2D diagram showing the laser discretization on the interface cells and the attenuated refracted ray. Each refracted ray is treated as an energy cuboid (the yellow rectangle in (B)) with a square section and the side length is the mesh size. The center of top surface of the energy cuboid is the center of the interface cell with a discretized incident ray, and the direction of the energy cuboid is the direction of the refracted ray. The length of the energy cuboid and the energy attenuation ratio along the length direction of the energy cuboid are determined by the attenuation coefficient γ . The energy of refracted ray is absorbed by the metal cells overlapped by the energy cuboid, i.e., the distance from the metal cell center to the refracted ray centerline d_v is smaller than the mesh size in this case. (C) 3D illustration of the overlapped volume of the metal cell and the energy cuboid of the refracted ray in three special cases. The vector \vec{d} shows the change path of d_v with the same vector of refracted ray \vec{v}_T . The linear increase of d_v will lead to the cubic growth, quadratic growth, and linear growth of the overlapped volume in the three special cases with constant unit vectors of $(\sqrt{3}/3, \sqrt{3}/3, -\sqrt{3}/3)$, $(\sqrt{2}/2, 0, -\sqrt{2}/2)$ and $(0, 0, -1)$, respectively. (For interpretation of the references to color in this figure legend, the reader is referred to the web version of this article.)

where $\cos\theta_1 = |\mathbf{n} \cdot \mathbf{v}_1|$ and e is the refractive index. \mathbf{C}_i and \mathbf{C}_j represent the cell center of Cell i and Cell j , respectively. d_{Rij} and d_{Tij} are the distance from Cell j ($i \neq j$) to the reflected ray and refracted ray at Cell i , respectively. \mathbf{v}_{Ri} and \mathbf{v}_{Ti} are the unit vector of the reflected ray and the refracted ray at Cell i , respectively.

In consideration of the energy of each refracted ray and reflection iterations, the ray tracing model is made compatible with the VOF method in this study according to the following five steps.

- (1) A vertical continuous laser beam is first discretized into multiple rays with a laser energy q_{10} (by Eq. (12)) for each column of the cells in z direction, as shown in the top arrows of Fig. 3B. q_{10} in Eq. (12) is a volumetric energy source term to convert the surface flux $P'(\Delta L)^2$ of laser energy into a volumetric source term by dividing the cell volume $(\Delta L)^3$ based on the assumption of uniform energy distribution in a CFD cell [21,53,71], where P' (Eq. (12)) is the laser energy per unit area. The ray exerted on each cell column is further discretized by the interface cells with an overall volume fraction ranging from 0 to 1 to render the reconstructed heated interface smooth and continuous between adjacent interface cells. The laser energy of the discretized ray at the metal–gas interface is $q_l = f_L q_{10}$. The laser absorption ratio f_L for each interface cell is calculated according to its overall volume fraction as compared with upper cells in z direction to satisfy the actual absorption order, i.e., the laser absorption ratio f_{Li} for interface Cell i is $\max\left\{\left(\alpha'_{li} - \max\left\{\alpha'_{lj}\right\}\right), 0\right\}$, where the coordinates of Cell i and j satisfy $x_i = x_j$, $y_i = y_j$ and $z_i < z_j$, as shown in the right side of Fig. 3A. The calculation scheme of absorption ratio is similar to the interface term $|\nabla\alpha_i|$ in the momentum equation (Eq. (20)), which transforms a surface force per unit area into a volumetric surface force [21,72,73].
- (2) For the interface Cell i with a ray energy $q_{li} > 0$ obtained from Step (1), the direction and energy of the reflected ray are calculated based on the Fresnel reflection. First, the energy of the reflected ray q_{Ri} for Cell i is calculated according to Eq. (13). The unit vector of reflected ray is calculated by Eq. (8) and the distance d_{Rij} from an interface Cell j ($i \neq j$) to the reflected ray is calculated by Eq. (11). If the interface Cell j satisfies the minimum distance $d_{ij} = |\mathbf{C}_i - \mathbf{C}_j|$ from Cell i to Cell j with $d_{Rij} < 0.5\Delta L$ and $\mathbf{v}_{Ri} \cdot \mathbf{n}_j > 0$, where ΔL is the mesh size and $\mathbf{v}_{Ri} \cdot \mathbf{n}_j > 0$ to avoid Cell i and Cell j being in the same side of the interface caused by the interface region, it will be selected as the next incident cell with a unit vector of incident ray equal to \mathbf{v}_{Ri} and an energy of incident ray equal to q_{Ri} for the next iteration of the Fresnel reflection and refraction. Note that the parallel computing for improving the computational efficiency should be switched back to serial computing when the new incident cell is determined as it may belong to different computing domain from the previous incident cell.
- (3) For the interface Cell i with a ray energy $q_{li} > 0$, the direction and energy of the refracted ray are calculated based on the Fresnel refraction [51]. First, the unit vector \mathbf{v}_{Ti} and energy q_{Ti} of the refracted ray for Cell i are calculated according to Eqs. (10) and (14), respectively. The schematic diagram for the discretized refracted rays of the interface cells at the metal–gas interface is shown in the left panel of Fig. 3B. Each discretized refracted ray is treated as an energy cuboid (the yellow rectangle in Fig. 3B) with an attenuated energy from the top surface to the bottom surface, as shown in the right panel of Fig. 3B. The center of the incident cell is taken as the center for the top surface, and the direction of the energy cuboid is the direction of the refracted ray. The length of the energy cuboid and the energy attenuation ratio along the length direction of the energy cuboid are determined by the attenuation coefficient γ . The attenuation coefficient γ varies with the metal state (solid or liquid), but it is simplified here as a constant for both solid state and liquid state due to lacking of reliable experimental data of Ti-6Al-4V. Existing absorption coefficient models [20,53,69,70] have assumed only the upper two to four cell (around $8 \sim 16 \mu\text{m}$) layers of the metal phase absorb the laser energy. An early study on polyimide [74] indicates that using a $6 \mu\text{m}$ for the interface region (around for his polyimide case) that absorbs the laser energy has the best performance compared with the experimental result. In this work, the attenuation coefficient γ is adopted at a value $0.192 \mu\text{m}^{-1}$ to ensure that the $10 \mu\text{m}$ thick interface layer and $16 \mu\text{m}$ thick interface layer can absorb most (85% for $10 \mu\text{m}$ and 95% for $16 \mu\text{m}$) of the ray energy. Advanced experiments are required in the future to calibrate the accurate value of the attenuation coefficient γ for Ti-6Al-4V with different states.
- (4) The energy q_P absorbed by the metal cells along the direction of the refracted ray is calculated based on the general Beer–Lambert form [75], which reflects the penetration of laser into the metal. The refracted ray starting from Cell i is treated as an energy cuboid obtained from Step (3) with a length of $25 \mu\text{m}$ and a side length of the square section of the mesh size ΔL in this case to reconstruct a smooth and continuous

energy absorption region. Such energy cuboid contains 99% of the energy of the refracted ray, as shown in the right panel of Fig. 3B. If the metal Cell j is overlapped by the energy cuboid, i.e., the distance $d_v = d_{Ti}$ (by Eq. (11)) from the metal cell center C_j to the refracted ray centerline v_{Ti} is smaller than the mesh size ΔL , the overlapped energy volume q_p (by Eq. (15)) will be absorbed by Cell j . C_e in by Eq. (15) is the ratio of the overlapped volume to the volume of Cell j . Notably, the calculation of the overlapped volume of a cuboid and a cube is rather complex. Assumptions are made for three special cases to simplify the consideration when constructing the equation of C_e . (a) $C_e = 1$ when the distance $d_v = 0$ for the refracted ray with any direction, implying that the whole Cell j can absorb the refracted ray energy when the refracted ray goes right through the center of Cell j . (b) $C_e = 0.5$ when the distance $d_v = 0.5$ for the refracted ray with arbitrary direction. This means that half of the Cell j can absorb the refracted ray energy when d_v is half of the mesh size ΔL . (3) $C_e = 0$ when the distance $d_v = 1$. A power function is applied to connect the three special cases and construct a continuous and smooth transition. The exponential k_T represents the sensitivity of distance d_v to the overlapped volume and the inclination of the refracted ray plays a key role in k_T , e.g., $k_T = 1$ when $v_T = (0, 0, -1)$, $k_T = 2$ when $v_T = (\sqrt{2}/2, 0, -\sqrt{2}/2)$ and $k_T = 3$ when $v_T = (\sqrt{3}/3, \sqrt{3}/3, -\sqrt{3}/3)$, representing a linear growth, quadratic growth and cubic growth of the overlapped volume with a linear increase of d_v and constant v_T , respectively, as shown in Fig. 3C. The energy density of Cell j is $(e^{-\gamma(l_{pij}-l_{oij})} - e^{-\gamma(l_{pij}+\alpha_{1j}\Delta L-l_{oij})}) q_{Ti}$, where l_{pij} is the distance between Cell i and Cell j and l_{oij} is the sum of the length occupied by the gas phase in the energy cuboid from Cell i to Cell j satisfying $l_{oij} = \sum_{l_{pik} < l_{pij}} C_e(1 - \alpha_{1k})\Delta L$ to guarantee only the metal phase can absorb the ray energy. Finally, a ray energy correction coefficient C_r is applied for each refracted ray to satisfy the energy conservation, i.e., the sum of absorbed energy of the metal cells along the refracted ray is equal to the energy of the refracted ray, and $C_{rij} = (q_{Ti} / \sum_j q_{pij})$, where i denotes the refracted ray from Cell i and j denotes Cell j that absorbs the ray energy.

- (5) The previous reflected ray from Cell i with the unit vector v_{Ri} and energy q_{Ri} is set as the new incident ray with the new incident cell with a center C_j , unit vector $v_{1j} = v_{Ri}$ and energy $q_{1j} = q_{Ri}$ obtained from Step (2). Steps (2) to (4) are then repeated until the energy of the reflected ray is weaker than a threshold percentage of its original energy (1% in this study). The final absorbed laser energy S_l is the sum of the energy absorbed by metal cells for all refracted rays and reflection iterations (by Eq. (16)).

The following summarizes the five equations used in aforementioned steps:

$$q_l = f_L q_{l0} = \frac{f_L P'(\Delta L)^2}{(\Delta L)^3} = \frac{2 P f_L}{\pi \left(R_0^2 + \left[\frac{\lambda(z-z_f)}{\pi R_0} \right]^2 \right) \Delta L} \exp \left[\frac{-2 \left[(x - X_1(t))^2 + (y - Y_1(t))^2 \right]}{R_0^2 + \left[\frac{\lambda}{\pi R_0} (z - z_f) \right]^2} \right], \tag{12}$$

$$q_R = \frac{1}{2} \left(\frac{1 + (1 - \varepsilon \cos \theta_1)^2}{1 + (1 + \varepsilon \cos \theta_1)^2} + \frac{\varepsilon^2 - 2\varepsilon \cos \theta_1 + 2 \cos^2 \theta_1}{\varepsilon^2 + 2\varepsilon \cos \theta_1 + 2 \cos^2 \theta_1} \right) q_l, \tag{13}$$

$$q_T = \left(1 - \frac{1}{2} \left(\frac{1 + (1 - \varepsilon \cos \theta_1)^2}{1 + (1 + \varepsilon \cos \theta_1)^2} + \frac{\varepsilon^2 - 2\varepsilon \cos \theta_1 + 2 \cos^2 \theta_1}{\varepsilon^2 + 2\varepsilon \cos \theta_1 + 2 \cos^2 \theta_1} \right) \right) q_l, \tag{14}$$

$$q_p = C_e (e^{-\gamma(l_p-l_0)} - e^{-\gamma(l_p+\alpha_1 \Delta L-l_0)}) q_T, \tag{15}$$

$$S_l = \sum_k \left(\sum_i \sum_j C_{rij} q_{pij} \right), \tag{16}$$

where f_L is the laser absorption ratio, ΔL is the cell size, P' is the laser energy per unit area, P is the laser power, R_0 is the laser beam radius, z_f is the z-coordinate of the lens focus, λ is the wave length of the laser, (x, y, z) is the coordinate of the calculated cell, and $(X_1(t), Y_1(t))$ represents the center of the scanning path in the x-y plane. ε is a material coefficient related to the electrical conductance [54,76], γ is the attenuation coefficient for

the laser penetration [75,77], and l_p is the distance from the incident cell of the refracted ray to the calculated cell. $C_e = 0.5(2 - 2d_v/\Delta L)^{k_T}$ when $\Delta L < 2d_v < 2\Delta L$ and $C_e = 1 - 0.5(2d_v/\Delta L)^{k_T}$ when $2d_v < \Delta L$, where $k_T = (|(\mathbf{v}_T)_x| + |(\mathbf{v}_T)_y| + |(\mathbf{v}_T)_z|)^2$ and the subscripts x , y and z represent three components of unit vector of the refracted ray \mathbf{v}_{T_i} in x , y and z directions, respectively. l_0 is the sum of the length occupied by the gas phase in the energy cuboid from the incident cell to the calculated cell. i represents the refracted ray from Cell i , j represents Cell j that absorbs the energy of the refracted ray starting from Cell i , and k represents the k th reflection iteration. C_r is the ray energy correction coefficient applied for each refracted ray to satisfy the energy conservation, as explained in Step (4).

2.4. Numerical aspects

The proposed computational approach is a significant extension of the semi-coupled resolved CFD-DEM method [53] recently developed by the authors. In the previous work, the method was employed to solve the powder motions, thermal field and fluid dynamics by considering mechanical interactions and heat transfers between the solid particles and viscous fluids. In this study, it has been greatly enriched by including the capability of modeling vapor and vaporization and melting materials, which is crucial for realistic SLM modeling. Following [53], we combine the fully resolved coupled CFD-DEM based on the Immersed Boundary (IB) method [78] to resolve the dynamics of fluids and the driven motion of powder grains, with a multi-phase CFD for solving the high-resolution thermal field of both fluids and solid grains by modeling a fictitious CFD domain occupying the actual physical space of a DEM particle. The use of fictitious CFD domain in the multi-phase CFD modeling helps to resolve the limitation in DEM modeling that one DEM particle can only have one single temperature rather than presenting an actual temperature gradient within the individual solid particle. This helps to avoid exceedingly complicated and costly treatments for each particle by DEM (e.g., by refining each particle to small elements [64]). Incorporation of the multiphase model further improves the accuracy and applicability of the semi-coupled resolved CFD-DEM with the consideration of the multiple solid material types and different phase change processes including fusion and vaporization.

Solid grains of possibly different materials are initially modeled as DEM particles distinguished as different particle groups with tagged temperatures. When their positions are settled after a CFD-DEM simulation of the layering process, the domains occupied by these DEM particles will be numerically replaced in a separate CFD domain by high viscous fluids with updated volume fraction with the same topology and physical parameters for the multi-phase CFD simulation of melting process when the temperature of a fraction of its fictitious CFD cells occupying the DEM particle is higher than the corresponding solidus temperature. An evaporation model with an inner boundary and a pressure drop equivalent to the Knudsen layer is further constructed based on the VOF method for the vaporization interface once the temperature of the melt flow cells is found reaching the boiling temperature. Two sharp interface capture schemes (isoAdvector and MULES) are applied for fluids with large velocity difference according to the Courant number. A VOF compatible ray tracing model considering the Fresnel reflection and refraction and the energy penetration as mentioned in last subsection is implemented to obtain an accurate thermal field for the fusion, vaporization and solidification of the metal. As such, all partial melting and full melting of powder grains and the vaporization of melt flow can be conveniently accommodated within this computational framework. Consequently, the semi-coupled resolved CFD-DEM with capability of modeling vaporization and multiphase materials is coined herein as the new *multi-phase semi-coupled fully resolved CFD-DEM*. Such a new computational model enables us to integrate multiple components and key physics dictating the dynamics of the melting process in SLM appropriately and rigorously.

2.5. Governing equations

Collectively, four sets of governing equations are simultaneously treated to solve the multiphase, multiphysics processes of SLM, including the linear and angular momentum equations for the motion of each granular powder particle, the continuity equation for the volume fraction field of multiple fluid phases, the fluid momentum equation based on the Navier–Stokes equation for the flow dynamics of multiple fluid phases and the temperature equation for the thermal field. We consider terms accounting for multiple physical phenomena, such as the surface tension, Darcy's effects, Marangoni's flow, recoil pressure and vapor pressure, in the fluid momentum equation, and the heat

transfer due to laser heat, conduction, dissipation, fusion, convection, radiation and vaporization in the temperature equation.

In the coupled CFD-DEM part of this method, the DEM is used to solve the following linear and angular momentum equations governing the motion of each granular powder particle:

$$\begin{cases} m_p \frac{d\mathbf{v}_p}{dt} = \mathbf{F}_f + m_p \mathbf{g} + \sum \mathbf{F}_{p-p} + \sum \mathbf{F}_{p-w} \\ I_p \frac{d\boldsymbol{\omega}_p}{dt} = \sum \mathbf{M}_t + \sum \mathbf{M}_r \\ \mathbf{F}_f = \sum_{j \in T_h} (-\nabla p + \mu \rho \nabla^2 \mathbf{u}_f)_j \cdot V_j, \end{cases} \quad (17)$$

where m_p and I_p denote respectively the mass and rotational inertia of Particle p . \mathbf{v}_p and $\boldsymbol{\omega}_p$ denote respectively the linear and angular velocities of Particle p . \mathbf{g} is the gravitational acceleration. \mathbf{F}_{p-p} and \mathbf{F}_{p-w} are the particle–particle interaction force and particle–wall interaction force [79,80], respectively. \mathbf{M}_t and \mathbf{M}_r are the torque from tangential force and rolling friction torque, respectively [81]. \mathbf{F}_f is the particle–fluid interaction force exerted on each particle of the DEM solver according to Shirgaonkar et al. [78]. p is the fluid pressure, \mathbf{u}_f is the velocity of the fluids, V_j is the volume of cell j , and T_h is the set of all particle-covered cells. Other interaction forces, such as inertial force, which may be important for specific applications [82], will be neglected in this study.

We consider multiple phases with an interphase mass transfer ratio \dot{m}_i in this simulation, such as the vaporization of melt flow into vapor, by assuming these flows to be incompressible and solved by the following advection equation.

$$\frac{\partial \alpha_i}{\partial t} + \nabla \cdot (\alpha_i \mathbf{u}_f) = \frac{\dot{m}_i}{\rho_i}, \quad (18)$$

where $\nabla \cdot (\mathbf{u}_f) = \sum \dot{m}_i / \rho_i$. Specifically, the continuity equation can be written as $\nabla \cdot (\mathbf{u}_f) = 0$ for an incompressible problem without any phase transformation. The subscript i represents different phases and α_1 , α_2 and α_3 represent the melt flow, metallic vapor and ambient gas in SLM. \dot{m}_i is the mass transfer ratio for phase i . A numerical term $\alpha_i \sum_j (\dot{m}_j / \rho_j) - \alpha_i \nabla \cdot (\mathbf{u}_f)$ is added to the RHS of Eq. (18) to improve the numerical stabilization when the implicit MULES scheme is used to solve the advection equation [61]. Only case of mass transfer due to the vaporization of melt flow into vapor is considered in this study. The mass transfer ratio \dot{m}_1 and \dot{m}_2 for the vaporized melt flow and the generated vapor in SLM can be written as [83,84]

$$\dot{m}_1 = -\dot{m}_2 = -0.54 p_0 \frac{\alpha_1}{\Delta L} \exp\left(L_v \cdot M \frac{T - T_{LV}}{RT T_{LV}}\right) \sqrt{\frac{M}{2\pi RT}}, \dot{m}_3 = 0. \quad (19)$$

The flow dynamics of multiple fluid phases during the melting process for SLM is assumed to be governed by the following momentum equation based on the Navier–Stokes equation. Note that the six terms on the RHS of Eq. (20) represent the surface tension, Darcy’s effects, Marangoni’s flow, recoil pressure, vapor pressure and pressure drop for the inner boundary, respectively.

$$\begin{aligned} \frac{\partial}{\partial t} (\rho \mathbf{u}_f) + \nabla \cdot (\rho \mathbf{u}_f \otimes \mathbf{u}_f) = & -\nabla p + \nabla \cdot (\mu \cdot (\nabla \mathbf{u}_f)) + c\sigma |\nabla \alpha_1| \frac{2\rho}{\rho_{\text{sum}}} \mathbf{n} \\ & -K_c \frac{(\alpha_1 - \alpha_m)^2}{\alpha_m^3 + C_k} \mathbf{u}_f + \frac{d\sigma}{dT} (\nabla T - \mathbf{n}(\mathbf{n} \cdot \nabla T)) |\nabla \alpha_1| \frac{2\rho}{\rho_{\text{sum}}} \\ & + 0.54 p_0 \exp\left(L_v \cdot M \frac{T - T_{LV}}{RT T_{LV}}\right) |\nabla \alpha_1| \frac{2\rho}{\rho_{\text{sum}}} \mathbf{n} + (\mathbf{F}_v + \mathbf{F}_{I.B.}), \end{aligned} \quad (20)$$

where p is the pressure and $p = p_d + \rho gh$, where p_d is the dynamic pressure, g is the gravitational acceleration, and h is the reference height [71]. c is the curvature of the fluid–gas interface, and $c = -\nabla \cdot \mathbf{n}$ where \mathbf{n} is the unit normal vector at the interface, $\mathbf{n} = \nabla \alpha_1 / |\nabla \alpha_1|$. σ is the coefficient of surface tension. $|\nabla \alpha_1|$ is an interface term to transform a surface force per unit area into a volumetric surface force [21,72,73]. ρ_{sum} is the sum of the density of phases at the interface, e.g., $\rho_{\text{sum}} = \rho_1 + \rho_2$ for a metal–vapor interface in SLM. $2\rho / \rho_{\text{sum}}$ is a sharp surface force term to smear out the interface [69,70]. K_c is the permeability coefficient, C_k is a constant to avoid division by zero, α_m is the volume fraction of the molten metal, T_l is the liquidus temperature, T_s is the solidus temperature, and L_v is the latent heat of vaporization. $d\sigma/dT$ represents the change of surface tension coefficient with temperature.

M is the molar mass, T is the temperature, T_{LV} is the boiling temperature, and R is the universal gas constant. F_v is the vapor pressure and $F_{1.B.}$ is the pressure drop applied on the inner boundary, as explained in Section 2.2. The following expressions are employed for the volume fraction of the molten metal α_m , metal viscosity μ and coefficient of surface tension σ that change with the temperature [20],

$$\alpha_m = \frac{\alpha_1}{2} \left[1 + \operatorname{erf} \left(\frac{4}{T_1 - T_s} \left(T - \frac{T_1 + T_s}{2} \right) \right) \right], \tag{21}$$

$$\ln \mu = \frac{1}{2} \operatorname{erfc} \left[\frac{4}{\ln T_1 - \ln T_s} \cdot \left(\ln T - \frac{\ln(T_1) + \ln(T_s)}{2} \right) \right] \cdot (\ln \mu_s - \ln \mu_1) + \ln \mu_1, \tag{22}$$

$$\sigma = \begin{cases} \frac{\sigma_1}{1 + \operatorname{erf} 2} \left[1 + \operatorname{erf} \left(\frac{4}{T_1 - T_s} \left(T - \frac{T_1 + T_s}{2} \right) \right) \right] & T \leq T_1 \\ \sigma_1 + \frac{\partial \sigma}{\partial T} T & T > T_1, \end{cases} \tag{23}$$

where μ_s and μ_1 are the viscosities at solidus temperature T_s and liquidus temperature T_1 , erfc is the complementary Gaussian error function. σ_1 is the surface tension coefficient of the metal at the liquidus temperature.

The thermal field is governed by the following temperature Eq. (24) derived from the energy conservation where the eight terms on the RHS of temperature equation in represent the heat transfer due to laser heat, conduction, dissipation, fusion, convection, radiation, vaporization, and energy correction for the generated vapor, respectively,

$$\begin{aligned} \frac{\partial}{\partial t} (C \rho_T T) + \nabla (C \rho_T T) \cdot \mathbf{u}_f &= S_1 + \nabla \cdot (k \nabla T) + \mu_T (\nabla \mathbf{u}_f + \mathbf{u}_f \nabla) : \nabla \mathbf{u}_f \\ &- L_f \left[\frac{\partial}{\partial t} (\rho_T \alpha_m) + \nabla \cdot (\rho_T \mathbf{u}_f \alpha_m) \right] \\ &- h_c (T - T_{\text{ref}}) |\nabla \alpha'_1| \frac{2C \rho_T}{(C_i \rho_i)_{\text{sum}}} \\ &- \sigma_{\text{sb}} (T^4 - T_{\text{ref}}^4) |\nabla \alpha'_1| \frac{2C \rho_T}{(C_i \rho_i)_{\text{sum}}} \\ &- 0.82 \frac{p_0 L_v M}{(2\pi M R T)^{0.5}} \exp \left(L_v M \frac{T - T_{LV}}{R T T_{LV}} \right) |\nabla \alpha'_1| \frac{2C \rho_T}{(C_i \rho_i)_{\text{sum}}} \\ &+ \phi_v, \end{aligned} \tag{24}$$

where L_f is the latent heat of fusion, h_c is the convective heat transfer coefficient, T_{ref} is the reference temperature, and σ_{sb} is the Stefan–Boltzmann constant. $(C_i \rho_i)_{\text{sum}}$ is the sum of the product of density and heat capacity of phases at the interface, e.g., $(C_i \rho_i)_{\text{sum}} = C_1 \rho_1 + C_2 \rho_2$ for a metal-vapor interface in SLM. ϕ_v is the energy correction term described in Section 2.2 for the generated vapor. S_1 is the laser input based on the ray tracing model [74] (see Section 2.3 and Eq. (16)) specially designed for the VOF method in this study.

2.6. Overall solution procedure

The proposed multi-phase semi-coupled resolved CFD-DEM approach has been implemented in two open-source codes, OpenFOAM and LIGGGHTS, in conjunction with the coupling engine *CFDEM* [85,86]. The VOF method with combined isoAdvector scheme and MULES scheme are coupled with the DEM to solve the multiphase, multi-physics problem for both the fluids and solid grains in SLM. A fictitious CFD domain composed of pure CFD fluids and virtual DEM particles is constructed to solve the high-resolution thermal field for all phases based on the energy equation. The IB method is combined with the Pressure Implicit with Splitting of Operators (PISO) to solve the velocity and pressure iteratively in CFD simulation [87] and the driven motions of the immersed grain bodies by DEM [88]. Key components of the proposed method have been validated by various test cases in early studies [89]. The PISO-IB scheme employed here is based on the one modified by Hager [90]. The complete solution procedure for the proposed multi-phase semi-coupled fully resolved CFD-DEM is summarized as follows, in conjunction with the flow chart shown in Fig. 4.

- (1) Prescribe the initial conditions for the CFD and DEM domains, including the volume fraction field, temperature field, pressure field, velocity field of fluids and the velocity, position, tagged temperature of particles.

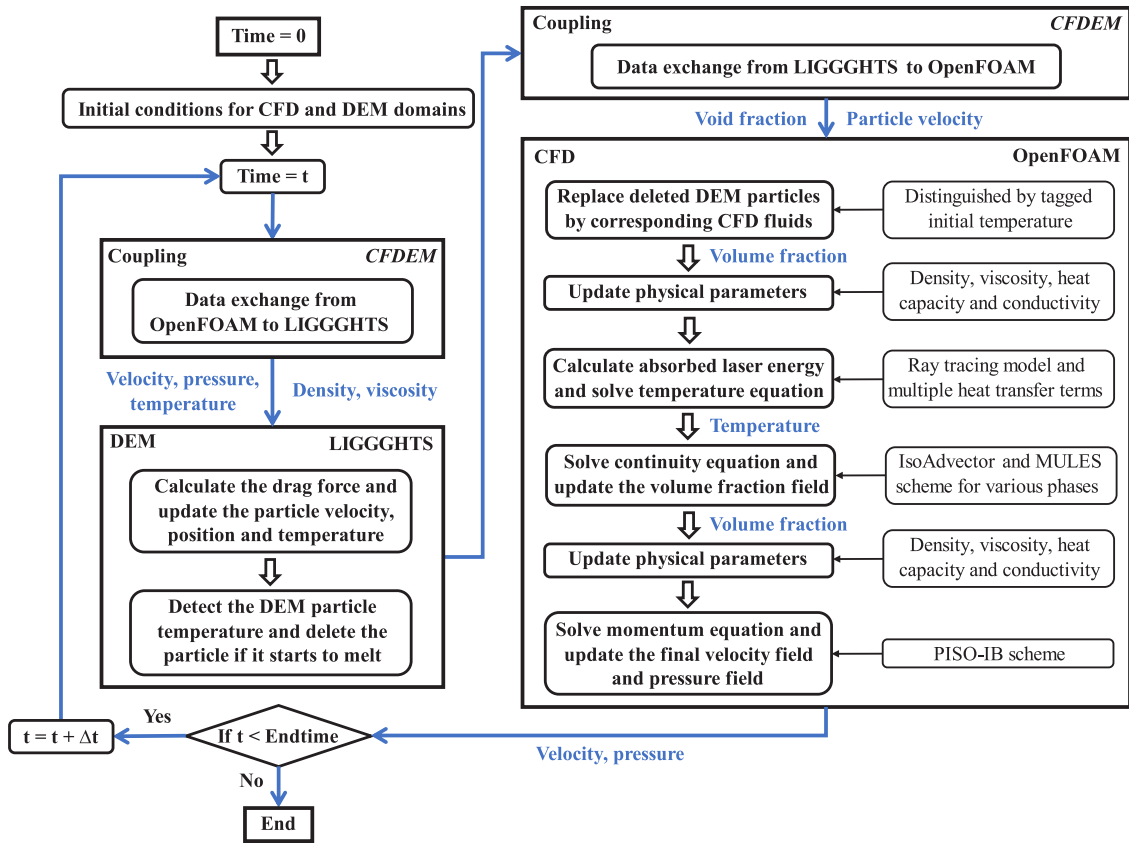


Fig. 4. Flow chat of the multi-phase semi-coupled resolved CFD-DEM method.

- (2) Update the particle motions by calculating the drag force acting on the particles and solving the linear and angular momentum equations in Eq. (17) [91]. The temperature of each cell in the particle domain is examined and the particle will be removed from the DEM if the temperature of any of its constituent cells exceeds its solidus temperature and meets the partial melting criterion.
- (3) Verify the change of both void fraction field to identify whether the DEM particle is removed in step (2) and to replace those deleted particles by CFD cells with identical temperature and material distinguished by the tagged temperature.
- (4) Update the physical parameters in Eq. (1) according to the volume fraction field and the temperature field, including density, heat capacity, thermal conductivity, and viscosity.
- (5) Calculate the absorbed laser energy in Eqs. (12) to (15) based on the ray tracing model that considers laser discretization, Fresnel reflection and refraction, and laser penetration, and solve the temperature equation (Eq. (24)) in CFD that considers the laser energy, six heat transfer terms due to dissipation, conduction, convection, radiation, fusion and evaporation, and the energy correction term for the generated vapor.
- (6) Choose a suitable sharp interface capture scheme for different phases according to the Courant number, update the mass transfer ratio based on the new temperature field and solve continuity equations in Eq. (18) to update the volume fraction field. Specifically, isoAdvector scheme is applied for the fluid phase that satisfies the CFL condition and MULES scheme is applied for other fluid phases with $CFL > 1$.
- (7) Update physical parameters in Eq. (1) according to the volume fraction field and temperature field, including density, heat capacity, thermal conductivity, and viscosity.
- (8) Update the velocity field \mathbf{u}_f and pressure field p_0 by solving the momentum equation in Eq. (20) that considers the buoyancy force, surface tension, Darcy's effects, Marangoni's flow, recoil pressure, vapor pressure, and pressure drop for the inner boundary, neglecting the existence of DEM particles. Correct the velocity field

and pressure field of the fluids according to the PISO-IB method in two steps: (a) Calculate \mathbf{u}_0 by correcting the old velocity field in the particle domain ($\mathbf{u}_0 = \mathbf{v}_p$) and the interface ($\mathbf{u}_0 = (1 - \varepsilon_p)(\mathbf{v}_p + \boldsymbol{\omega}_p \times \mathbf{r})$, where ε_p is the void fraction, \mathbf{v}_p and $\boldsymbol{\omega}_p$ denote respectively the linear velocity and angular velocity of the particle, \mathbf{r} is the position vector of the particle). (b) Further correct the velocity field \mathbf{u}_0 according to $\mathbf{u} = \mathbf{u}_0 - \nabla\phi$, where $\nabla^2 \cdot \phi = \nabla \cdot \mathbf{u}_0 - \sum \dot{m}_i / \rho_i$, to satisfy the mass conservation $\nabla \cdot (\mathbf{u}_i) = \sum \dot{m}_i / \rho_i$ where \dot{m}_i and ρ_i denote the mass ratio (Eq. (19)) and density of phase i , respectively. Then update the pressure p_0 using $p = p_0 + \rho \cdot \nabla\phi / \Delta t$.

(9) Go to step (1) to repeat the simulation until the final time step is reached.

3. Numerical simulation of SLM

3.1. Parameter selection and model setup

The melting process of SLM with typical titanium alloy Ti-6Al-4V powders is considered to examine the predictive capability of the proposed computational framework. Relevant physical parameters are shown in Table 1 and grain size distribution of the Ti-6Al-4V powder can be found in our previous paper [53] which will not be listed here to save space. The atmospheric pressure p_0 is 101 kPa and the laser diameter is 95 μm according to experimental data [92]. Temperature-dependent thermal parameters [93,94] for the Ti-6Al-4V, ambient gas (i.e., Argon gas) shown in Table 2 are adopted to render more realistic simulation results [20]. The following temperature dependent density, heat capacity, the thermal conductivity of Ti-6Al-4V and Argon gas, the viscosity of Argon gas, and the density of Ti-6Al-4V vapor derived from the ideal gas law are adopted. The thermal conductivity, heat capacity and viscosity of the Ti-6Al-4V vapor are selected as 0.05 W/(m K), 717 J/(kg K) and 0.00024 Pa s, with reference to the NIST Chemistry WebBook [95] and the data of Cesium vapor [96], Lithium vapor [97] and Argon gas [93] due to the loss of Ti-6Al-4V vapor information in previous studies.

In simulating the SLM of Ti-6Al-4V powders on bare plate or powder bed, we choose a grid size of 4 μm for the CFD based on convergence study of our previous work [53]. The grid size for the bare plate in SLM is set as 5 μm as there is no need to consider DEM coupling with CFD for the plate so that the cell size will not be restricted by the IB method [20]. A Cyclic Arbitrary Mesh Interface (AMI) [61] boundary is further employed to expand the CFD domain to account for vapor/gas expansions. An extra domain composed of vapor and ambient gas only with a coarse grid size of 10 μm is added to the original domain when needed to fetch a balanced between computational efficiency and accuracy. Such added domains can be identified in the subsequent simulations in Figs. 11, 12, and 13, by the high velocity vectors of the vapor and gas. The time step chosen for CFD is 4×10^{-8} s, which is ten times of the corresponding time step for the DEM simulation (i.e., 4×10^{-9} s). The bottom boundary is set to be a non-slip wall with zero gradient for pressure, and other boundaries are set as fixed value for pressure and zero gradient for velocity and temperature. A substrate ranging from 100 μm to 300 μm in thickness, depending on the laser power, is considered for the SLM simulation in expecting that deep keyholes may be induced by stronger laser powers. The bottom boundary of the substrate is set to be zero gradient for temperature, as shown in Fig. 5.

3.2. Model validation

Three validation cases with stationary laser illumination are conducted to validate three key components of our numerical model. The VOF compatible ray tracing model is validated based on the evolutions of melt pool and vapor depression in a bare plate case under stationary laser illumination (Fig. 6), which is a typical benchmark in published studies [54,55,74] for the laser absorption model. One capability of our model is to convert particles to a partially melted state when the temperature of a cell in the particle reaches the solidus temperature, which is validated by the following simple case (Fig. 7) with a single particle and plate, and the conversion of moving DEM particles can be found in Fig. 8D (P2 and P3). A quantitative comparison of the powder trajectory and the corresponding velocity change between experiments [52] and our simulation results is made to validate the proposed semi-coupled resolved CFD-DEM with the implemented evaporation model.

Four stages of the evolutions of melt pool and vapor depression in a bare Ti-6Al-4V plate under stationary laser illumination have been observed by Cunningham etc. [92], as shown in Fig. 6A. In the first stage, the vapor depression is formed and continues to grow steadily, leading to a quasi-semicircular melt pool (a-c). With further development of the vapor depression further grows, and the melt pool shape becomes sharper at the tip of the

Table 2

Temperature-dependent thermal parameters of Ti-6Al-4V, argon gas and Ti-6Al-4V vapor.

Material	Parameter and units	Value or equation
Ti-6Al-4V	Density (kg/m ³)	$\rho_{\text{Ti64}} = \begin{cases} 4420 & T < 1268 \text{ K} \\ 4420 - 0.154(T - 298) & 1268 \text{ K} < T < 1923 \text{ K} \\ 3920 - 0.680(T - 1923) & T \geq 1923 \text{ K} \end{cases}$
	Heat capacity (J/(kg K))	$C_{\text{Ti64}} = \begin{cases} 411.5 & T < 1268 \text{ K} \\ 411.5 + 0.2T + 5 \times 10^{-7}T^2 & 1268 \text{ K} < T < 1923 \text{ K} \\ 830 & T \geq 1923 \text{ K} \end{cases}$
	Thermal conductivity (W/(m K))	$k_{\text{Ti64}} = \begin{cases} 19.0 & T < 1268 \text{ K} \\ -0.80 + 0.018T - 2 \times 10^{-6}T^2 & 1268 \text{ K} < T < 1923 \text{ K} \\ 33.4 & 1923 \text{ K} < T < 1973 \text{ K} \\ 34.6 & T \geq 1973 \text{ K} \end{cases}$
Argon gas	Density (kg/m ³)	$\rho_{\text{Argon}} = 745.2 \times T^{-1.05}$
	Heat capacity (J/(kg K))	$C_{\text{Argon}} = 500$
	Thermal conductivity (W/(m K))	$k_{\text{Argon}} = 0.00668 + 0.000048 \times T$
	Viscosity (Pa s)	$\mu_{\text{Argon}} = 5.2 \times 10^{-7} \times T^{0.68}$
Ti-6Al-4V vapor	Density (kg/m ³)	$\rho_{\text{Vapor}} = 4685.5 \times T^{-1.05}$

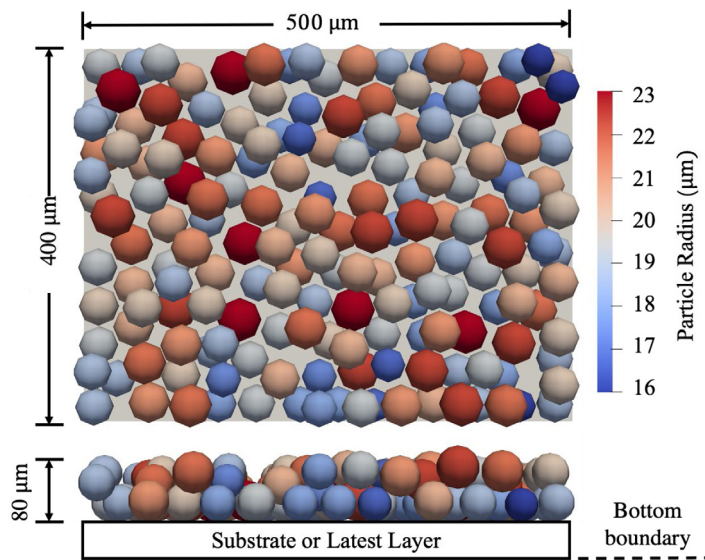


Fig. 5. Model setup for coupled CFD-DEM simulations of SLM with Ti-6Al-4V alloy powder. The length, width and thickness of the Ti-6Al-4V alloy powder layer is 500 μm, 400 μm and 80 μm respectively.

vapor depression with instabilities in the second stage (d-f). Interesting periodic fluctuations could be observed in the third stage (f-h) as the vapor depression penetrates at a much faster rate into the material. In the final stage, a deep keyhole is formed with a spike in the middle of the bottom and the keyhole strongly fluctuates (i-j) with the continuing stationary laser illumination. Notably, the observed four stages in experiments can be effectively captured

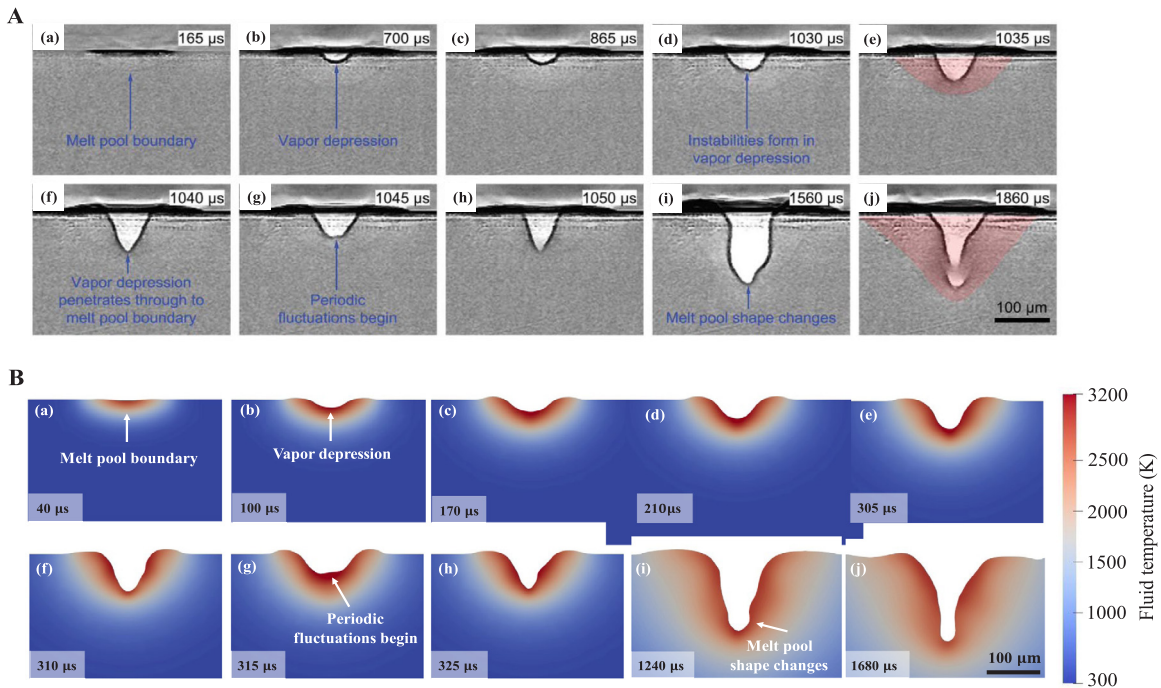


Fig. 6. Comparison between experiments results [92] (A) and simulation results (B) of evolutions of melt pool and vapor depression under stationary laser illumination. (a-c) Formation and steady growth of the vapor depression. (d-f) Formation of instability in vapor depression and further growth of the vapor depression. (f-h) Formation of periodic fluctuation of the vapor depression. (i and e) Change of the melt pool shape and further fluctuation of the vapor depression with the increasing keyhole depth. The laser power is 156 W and the laser spot size is 140 μm .

by our numerical model, as shown in Fig. 6B, partially proving the accuracy of the proposed VOF compatible ray tracing model. Note that the time sequence may not be perfectly matched for the four stages between numerical the experimental tests since a constant energy attenuation coefficient has been adopted in our numerical model while it may be different in the metal state [98] where the attenuation in solid metal is extremely fast. The attenuation coefficient for different metal states will be subject to further study in the future in conjunction with the dynamics and detailed physical mechanisms of the vapor depression stabilities and strong fluctuations.

A second validation case is shown in Fig. 7 which presents a complete melting and vaporization process for a single Ti-6Al-4V powder over a Ti-6Al-4V substrate simulated by our proposed numerical model. The laser power used in the simulation is 200 W and the laser spot size is 150 μm . In the initial stage ($t = 0 \mu\text{s}$), the Ti-6Al-4V powder is modeled by the DEM particle. An equivalent void fraction field, i.e., the fictitious CFD domain, is constructed according to the particle position (Fig. 7A). The temperature field is resolved by combining the original CFD domain and the fictitious CFD domain. The temperature distribution in the DEM particle can be represented by the temperature field of the fictitious CFD particle built upon the void fraction field, as shown in the right panel of Fig. 7A. The DEM particle is deleted and replaced by the CFD fluid particle (Fig. 7B) when the temperature of any cell in the DEM particle is higher than the solidus temperature, e.g., between 5.6 μs and 5.7 μs in this case. A CFD fluid particle with identical shape and temperature field with the DEM particle is derived from the fictitious CFD particle (Fig. 7B) to guarantee the accuracy of the deletion and replacement process. Khairallah etc. [8] compared the melting process using two laser absorption models, namely, the homogeneous laser deposition and laser ray tracing, shown in Fig. 7C their respective temperature fields predicted for the single particle case during the melting process. The wetting contact with the substrate increases rapidly for homogeneous laser deposition as the energy is uniformly distributed in the particle such that melting occurs simultaneously everywhere inside the particle, whereas the melting portion of the particle is released to the substrate gradually through a narrow point contact (Fig. 7C) by the ray tracing prediction as melting occurs first at the particle surface. Our simulation results can reproduce the same melting phenomenon as the ray tracing model by Khairallah etc. [8] as shown in Fig. 7D.

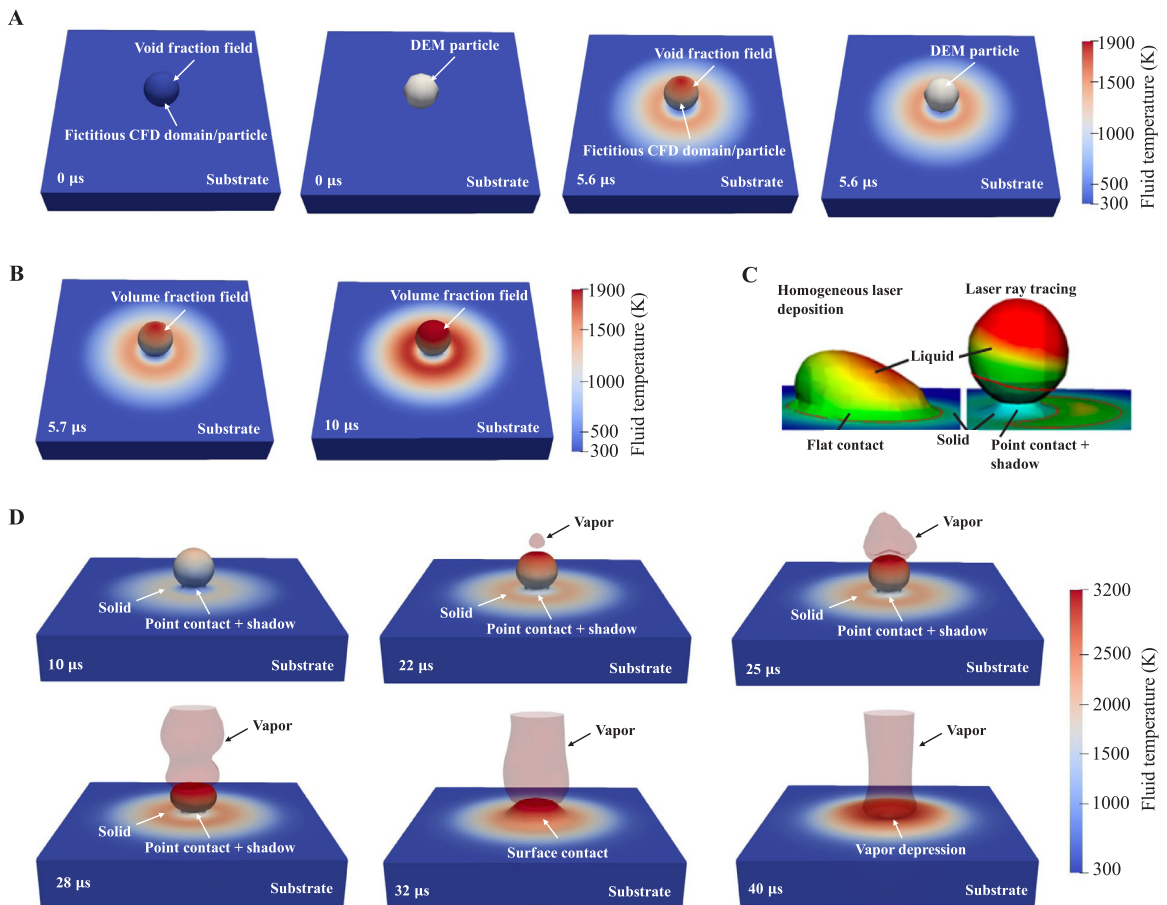


Fig. 7. Numerical simulations of the melting and vaporization process of a single Ti-6Al-4V powder and Ti-6Al-4V plate under stationary laser illumination (A, B, D) in comparison with numerical simulations of single particle melting process with two laser absorption method published in the literature [8] (C). (A) The position of DEM particle and the temperature field of the equivalent void fraction field ε_p (fictitious CFD domain) at $0 \mu\text{s}$ and $5.6 \mu\text{s}$. (B) The temperature field of the volume fraction field α_1 at $5.7 \mu\text{s}$ and $10 \mu\text{s}$. The DEM particle is deleted and replaced by the fluid particle between $5.6 \mu\text{s}$ and $5.7 \mu\text{s}$ with the same shape and temperature field based on the previous void fraction field as one cell in DEM particle reaches the solidus temperature after $5.6 \mu\text{s}$. (C) The temperature field using the homogeneous laser deposition method and the laser ray tracing method predicted in [8]. The melting happens simultaneously everywhere inside the particle for the homogeneous laser deposition, and the melting occurs first at the particle surface for realistic laser ray tracing [8]. (D) Melting process and temperature field of our numerical model match the results of the case using laser ray tracing method in (C). Vaporization happens with the increasing temperature when the temperature reaches the boiling temperature. The laser power is 200 W and the laser spot size is $150 \mu\text{m}$. The particle diameter is $40 \mu\text{m}$ and the mesh size is $4 \mu\text{m}$. The interfaces of the void fraction field, metal phase and vapor phase shown in the figure are $\varepsilon_p = 0.5$, $\alpha_1 = 0.5$ and $\alpha_2 = 0.2$, respectively. Since the vapor phase is always mixed with the ambient gas, a small interface value is chosen here to consider the ambient gas–vapor mixture.

The upper side of the particle that absorbs the laser energy melts first and moves downward through a point contact ($10 \mu\text{s}$ – $28 \mu\text{s}$ in Fig. 7D) due to the gravity and the recoil pressure caused by the generated vapor. The point contact is further converted to a surface contact at $32 \mu\text{s}$ as the particle is fully melted and vapor depression occurs at $40 \mu\text{s}$ with the continuing stationary laser illumination. Our numerical model is capable of providing a transition from the DEM particle to the CFD fluids at the solidus point during which such information as the shape and temperature field of the DEM particle can be accurately transferred to the corresponding CFD fluid particle to guarantee the numerical accuracy and consistency. Further melting process is solved by the multi-phase CFD, which is similar to most published studies [21,71,83].

A third validation case is presented for the prediction of particle movements in the melting process. Fig. 8 presents the predicted trajectories and the corresponding velocity changes of three tagged powders by our simulation in

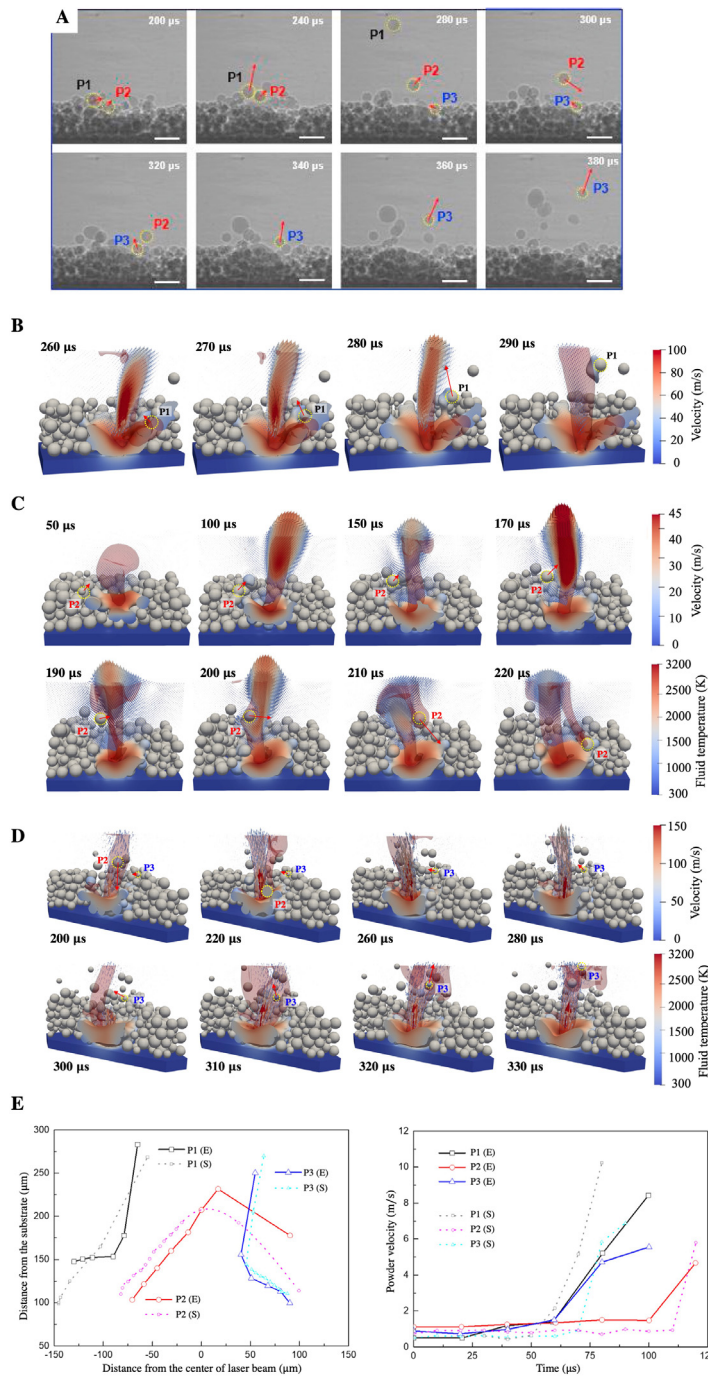


Fig. 8. Comparison between experiments [52] and our simulations on powder motion during the melting process. (A) Time sequence of X-ray imaging with three tagged powders observed in the experiments [52]. (B–D) Simulation results with three tagged powders based on comparable setups as the experiments [52]. (E) The trajectories and velocity versus time of three tagged powders in (A–D). P1 (E) denotes Powder P1 in the experiments and P1 (S) denotes Powder P1 in the simulations. The time in E is a relative one rather than the absolute time as in experiments or simulations to make the results comparable and the curves in E are reproduced from [52]. The laser power used is 160 W, the laser spot size is 150 μm , the powder layer thickness is 140 μm , and the substrate thickness is 40 μm . The powder size is 9–56 μm and the mesh size is 4 μm . Different sections are selected to render better observations on the tagged particle movement in (B–D).

comparison with experimental observations [52]. Powder particles P1 and P3 represent typical surrounding powders entrained by the high-speed vapor generated during the melting process. They move to the center of the laser beams with a small velocity (around 1 m/s) in the initial stage. With their distance from the laser beam center reduced, their velocities increase rapidly due to the stronger drag force caused by the entrained ambient gas. In the second stage, these particles are further lifted and driven by the high-speed vapor and ambient gas, moving upwards with a velocity larger than 5 m/s (Fig. 8E). Different from Powders P1 and P3, Powder P2 can pass through the laser beam center in conjunction with an obvious change of moving trajectory and a significant increase of velocity when it approaches closer to the laser beam center. In this simulation case, the laser power used is 160 W, the laser spot size is 150 μm , the powder layer thickness is 140 μm , and the substrate thickness is 40 μm . Evidently, our simulation results can reasonably capture the same trends of trajectories and the corresponding velocity changes as observed in the experiments. In consideration of and the random powder distribution, the observed discrepancies are acceptable (Fig. 8E). Fig. 9(B–D) present the velocity field of high-speed vapor and the entrained ambient gas and powders, further confirming the increasing drag forces acted on the powders near the vapor region. The velocity of vapor decreases significantly (190 μs – 220 μs in Fig. 9C) when Powder P2 passes through the laser beam center or the vapor, as Powder P2 directly absorbs part of the laser energy, leading to a temporary drop of temperature for the melt pool underneath P2. The lift force from the weakened vapor in conjunction with the drag force forms an entrained ambient gas with an increasing downward velocity (190 μs in Fig. 9C), causing Powder 2 to fall. Note that the time sequence of powder motion is not matched with experiments, similar as in Fig. 6, which may have been caused by the constant energy attenuation coefficient adopted in this model and merits a further study in the future. The combination of the implemented evaporation model and the semi-coupled resolved CFD-DEM is shown to be capable of capturing powder motions under high-speed vapor and entrained ambient gas in a reasonable manner. Detailed dynamics and physical mechanisms of the complex interactions among ambient gas, metal vapor, powders, and melt flow require more quantitative study in the future.

3.3. Capturing the full picture of melt pool dynamics in SLM of Ti-6Al-4V alloy powders

The proposed computational framework is first employed to simulate the melting process of SLM with typical titanium alloy Ti-6Al-4V powders. Major challenges for both experimental observation and theoretical prediction of the melting process of SLM include the multiple phase transformations that manifest intricate, highly dynamic intra- and inter-phase interactions. These features contribute critically to the melt pool dynamics, the understanding of which is pivot to quantitatively evaluate and control the quality of melt track and built part in terms of surface roughness, ripples on the melt track, partially melted powders and discontinuity between two tracks [53]. As an opening summary of the subsequent specific results on SLM, we use Fig. 9 to show a complete picture captured from our numerical simulation that includes all the aforementioned ingredients during a SLM of titanium alloy Ti-6Al-4V powders over a thick plate. Evidently, this simulation identifies the high-speed vapor, the deep keyhole formation, the entrained ambient gas that forms vortex flow (see zoomed inset on the left) and drive the surface powders to spatter or scatter. The inset also shows how the vapor and swirled ambient gas work together to form the surface flow pattern for the melt pool. In what follows, further simulation cases will be presented to highlight the individual facet of melt pool dynamics in Fig. 9 for quantitative physical interpretations, many for the first time to the knowledge of authors. In particular, the proposed computational tool will be shown capable of capturing three forms of phase transformation: (1) melting of solid grains into liquid; (2) vaporization of melt flow into metallic vapor; and (3) solidification of melt flow into solidified melt track. These phase transformations involve intricate interactions among four phases of solid grains, melt flow, metallic vapor, and ambient gas. Shown also are the conditions under which the melt pool dynamics renders fluctuated surface solidification and hence increased surface roughness. We also show how the dynamics of melt pool in conjunction with high-speed vapor may cause scattering and splashing of the solid grains during laser scanning.

3.4. Melt pool morphology in SLM of Ti-6Al- 4V bare plate

Fig. 10 presents selected representative simulations in comparison with their corresponding experimental observations [92] on the melt pool morphology for laser scanning of a Ti-6Al-4V bare plate at various laser power and scanning velocity. As shown in Fig. 10A and B, the numerical predictions of melt pool profiles for the eight

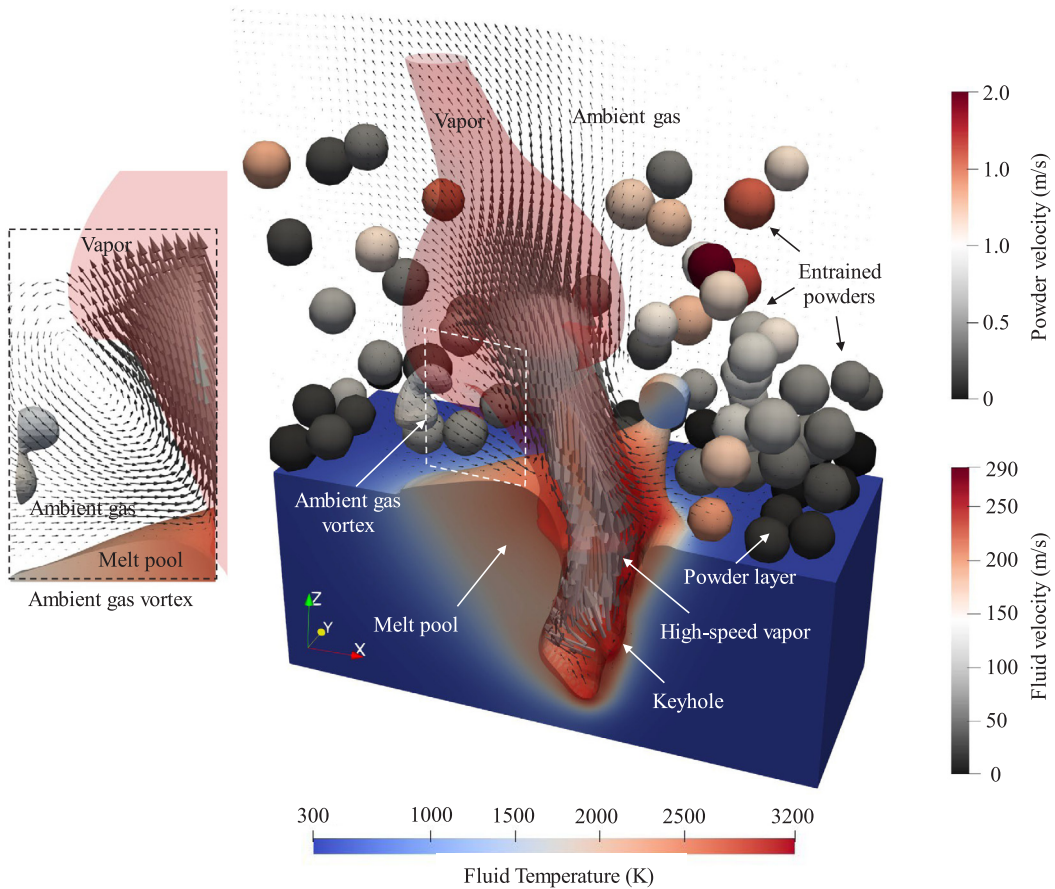


Fig. 9. Physically based, high-fidelity numerical simulation based on multi-phase, semi-coupled resolved CFD-DEM captures a complete profile of metallic powder-based SLM including all ingredients of a typical melting process: the melt pool, deep keyhole, ambient gas, high-speed vapor, powder layer and entrained powders. The cross sections of the melt pool and powders are selected to show the melt pool, keyhole and the vapor more clearly. Shown in the magnified inset on the left is the ambient gas vortex caused by the high-speed vapor (with foreground powders removed for better illustration) at the ambient gas–vapor interface. The simulation case has been performed on Ti-6Al-4V powder layers overlaying a thick plate subjected to laser illumination with a laser power of 280 W and a scanning velocity of 70 cm/s.

cases with different combinations of laser power and scanning velocity, ranging from 156 W to 416 W and from 40 cm/s to 120 cm/s, respectively, compare reasonably well the corresponding experimental radiographs on the formation of keyholes (or vapor-filled depressions) [92]. The velocity fields of melt pool liquid shown in Fig. 10B also reveal its dynamic nature agitated by the high-speed, high-temperature vapor in shaping the final morphology of melt track and possible formation of defect pores. A further quantitative examination of keyhole depth and the front keyhole wall angle, as shown Fig. 10C and D, confirms that both have a positive linear correlation with the laser power and an inversely proportional correlation with the scanning velocity, which is consistent with experimental radiograph observations and quantitative test data [92]. Future studies may be directed toward finding a properly defined laser power density by combining the laser power and scanning velocity (e.g., via their ratio) to establish a direct correlation with the keyhole depth and front keyhole wall angle. Fig. 10D further confirms our numerical data points compare well with the linear experimental fitting line between keyhole depth and front keyhole wall angle. The high consistency between our simulation results and the experimental data validates our numerical model for providing reliable predictions on keyhole formation under combined influence of laser power and scanning velocity.

The keyhole formation in SLM is indeed found a highly dynamic, unstable process which is significantly affected by the high-speed vapor. While the front keyhole wall may maintain a relatively steady angle, its back wall depicts a highly dynamic oscillation feature as a result of the intense interaction between the metal vapor and the melt

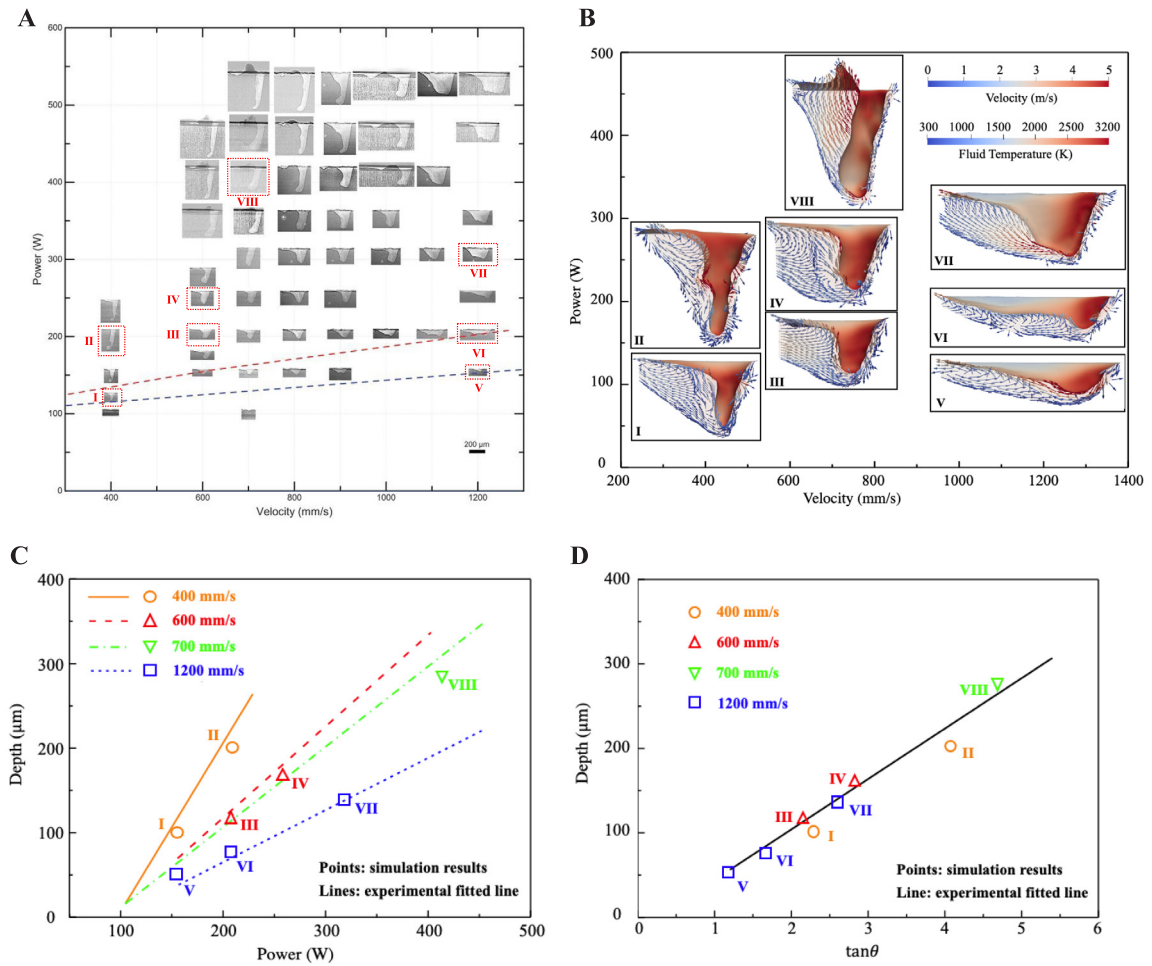


Fig. 10. Numerical simulations of the melt pool morphology compare quantitatively well with experimental observations and data [92]. (A) Experimental observation of keyhole morphologies in P-V space [92], where P is laser power and V is scanning velocity. The eight cases (I–VIII) marked in the figure in windows are selected for comparison with numerical simulations. (B) Simulated keyhole morphology (in red contour of temperature) in melt pool (shown by the flow velocity vectors formed in the melt pool around the keyhole) for cases I to VIII in the P-V space marked in (a). The eight cases selected for simulations are (scanning velocity [mm/s], laser power [W]): I (400, 156), II (400, 208), III (600, 208), IV (600, 260), V (1200, 156), VI (1200, 208), VII (1200, 312), and VIII (700, 416). (C) Correlation of simulated keyhole depth versus laser power for Case I to VIII (symbols) with experimental fitted line [92] (solid lines). (D) Correlation of simulated keyhole depth versus front keyhole wall angle θ for Case I to VIII (symbols) with experimental fitted line [92] (solid line) in depth- $\tan\theta$ space. (For interpretation of the references to color in this figure legend, the reader is referred to the web version of this article.)

flow. In particular, the driver of the dynamic keyhole structural characteristics is the high-speed, high temperature vapor which is kept generated by the laser from the front wall of the keyhole, as will be discussed below. Future studies of keyhole formation should place a focus on experimental determination of physical parameters for the generated vapor and its dynamic properties interacting with the surrounding melt liquid. The availability of such data will further help to improve both the consistency and accuracy for the proposed multiphase semi-coupled resolved CFD-DEM approach in simulating keyhole formation of SLM.

3.5. Dominant high-speed vapor flow dictating keyhole formation and surface melt flow

The incorporation of vaporization of melt flow and vapor dynamics with ray-tracing model for laser power in our approach empowers us to simulate and capture how the generated high-speed, high-temperature vapors interact

with the melt pool liquid during the melting process and provide a dominant driving force for dynamic melt pool evolution. Presented in Fig. 11 are three simulated cases showcasing such interactive mechanism. The generated vapor shown in Fig. 11A and B for Case VI, at a scanning velocity of 1200 mm/s and laser power of 208 W, is found to escape at a speed in excess of 250 m/s from within the front keyhole wall and travel up and backwards relative to the scanning director, an observation consistent with the experiment reported by Bidare [6]. In Case II where the scanning velocity is slow at 400 mm/s with the same laser power (Fig. 11D), the escaping vapor travels up from a deeper keyhole roughly along the vertical direction at an even higher speed as compared to Case VI. For Case VIII (Fig. 11C) where the scanning velocity is at 700 mm/s with a high laser power of 416 W, the dynamic oscillation of the keyhole may render the vapor travels temporarily forward to the scanning direction before escaping upwards from the keyhole, entraining the ambient gas along its route to cause intricate vortex structures. Due to its sustained interaction with the melt flow inside the keyhole as seen in Fig. 11C, the maximum vapor speed in Case VIII is less than half of that observed in both Case II and Case VI.

The vapor–gas vortex structure formed in the vicinity of melt pool liquid accounts directly for the evolution of the surface melt flow pattern that affects the surface characteristics of melt track. Presented in Fig. 11 (B–D) are three typical ground flow patterns of the melt pool (see also the magnified insets) for cases VI, VIII and II, coined here as flat, convex bump, and inclined flow shapes, respectively. Fig. 11E shows the ratio of surface drag force caused by the high-speed vapor flow to the Marangoni's force along the center interfaces of three typical flow patterns. Due to high scanning velocity, the vapor depression zone formed in Case VI is shallow (Fig. 11B), which allow relative more volume of melt liquid to be mobilized. The vapor generated in this case, without a backwall like in the keyhole cases to divert either its direction or slow it down, travels backwards nearly along the ground surface at a rather high speed. It produces moderate surface drag, around 25% of the Marangoni's force (Fig. 11E), to the melt liquid that overpowers the mild vapor–gas interface vortex and pulls the liquid to travel long distance before it slows down and builds up at the plate surface to form a mild bump. This is how the relative flat surface with mild bump far behind pattern is formed for Case VI (Fig. 11B). In Case VIII (Fig. 11C), a relatively vertical vapor flow escaping from the deep and relative uniform keyhole drags the melt flow upwards, leading to a strong surface drag force larger than the Marangoni's force up to triple or quadruple times (Fig. 11E); strong vortexes formed at the vapor–gas interface right behind the melt pool trigger a circulation mechanism to push the melt liquid from flowing backward and the drag force increases rapidly to reach a value tripling of that of the Marangoni's force from the bottom to the top of the convex part (Fig. 11E). The two mechanisms work together to form a sharp bump surface for this case, where the vortex circulation renders a concave back and convex form shape for the bump (Fig. 11C). In addition to the vortex near the melt pool, two vortices are also found on both sides of the fast-moving vapor flow in Fig. 11C and this phenomenon has been reported in a previous study [13]. The vortex in Case II is relatively weak, causing a surface drag force smaller than 5% of the Marangoni's force (Fig. 11E). The vapor escaping from a deep and 'V'-shaped keyhole travels fast along vertical direction tilting backwards. They combine to push small volume of melt liquid and form a slightly inclined melt pool surface with the Marangoni's effect (Fig. 11D).

3.6. Dynamic correlation between melt pool evolution and vapor circulation

To further examine how high-speed vapors dictate the evolution of melt pool during the melting process, we present in Fig. 12 a comparison of the sequential change of melt pool observed by high-speed X-ray imaging (Fig. 12A) [92] with our numerical simulations (Fig. 12B, C) for Case III (with a laser power at 520 W and scanning velocity at 700 mm/s) where a good consistency can be observed. It is striking to see the clear correlation between the vapor circulation with the variation of the keyhole morphology and the overall melt pool evolution. The high-speed vapor generated along the front keyhole wall travels backwards and downwards to depress the keyhole (Stage 2 in Fig. 12B) and further circulate upwards after interacting with the back wall of the keyhole (see inset of Fig. 12C), causing volumetric expansion of the keyhole to form a bulging tummy at the back wall of the keyhole (see Stage 3 in Fig. 12B). The circulated vapor joins the vapor generated at shallow depth to form an upward escaping vapor flow (see inset of Fig. 12C). This vapor circulation is unsteadily interacting with the keyhole both the keyhole walls that set a boundary between the keyhole vapor and the melt pool liquid. In conjunction with Fig. 12B, it is noticed that the drag of upward circulating vapor constantly results in an upward flux of melt pool liquid behind the back wall of the keyhole, pushing up a continuous, yet unsteady supply of melt liquid to emerge to the surface. The newly pumped-up liquid merges with the original bump and collapses backwards due to both

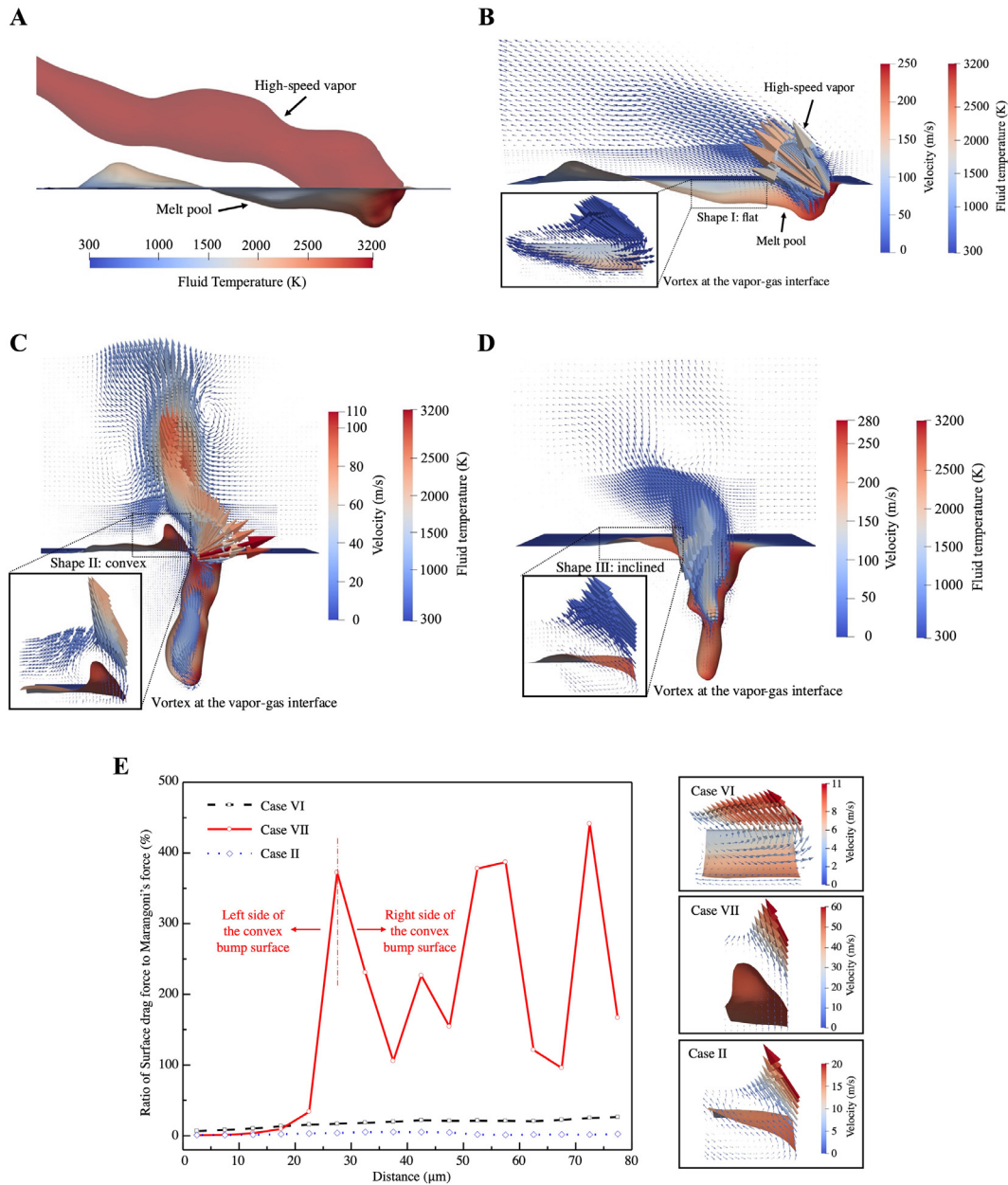


Fig. 11. Simulated melt pool surface in relation with generated vapor and ambient gas flows for cases VI (A, B), VIII (C) and II (D). (A) Case VI: the melt pool and generated high-speed vapor during the laser scanning. (B) Case VI: central cross-section profile of the melt pool and velocity vector contour of vapor and ambient gas. (C) Case VIII: Central cross-section profile of the melt pool and the velocity vector contour of vapor and ambient gas. (D) Case II: central cross-section profile of the melt pool and the velocity vector contour of vapor and ambient gas. Three typical shapes of the back part of the melt pool as well as the corresponding velocity field can be found in (B), (C) and (D), presenting as flat, convex bump, and inclined surfaces, respectively. (E) The ratio of surface drag force caused by the vapor flow to the Marangoni's force along the selected interface in the center longitudinal cross section of cases VI, VII and II. Three selected interfaces and their corresponding velocity fields are shown in the right panel. The length of each selected interface is $80\ \mu\text{m}$, represented by 16 CFD cells, and the x coordinate (Distance) starts from the left side of the selected interface. The first $27.5\ \mu\text{m}$ represents the left side of the convex bump surface and other $52.5\ \mu\text{m}$ represents the right side of the convex bump surface. The Marangoni's force and the surface drag force are calculated based on the Marangoni's term and the viscous term in Eq. (20) respectively. Large curve fluctuations occur in the right side of the convex bump surface due to small temperature difference at the surface and the nonlinear temperature field.

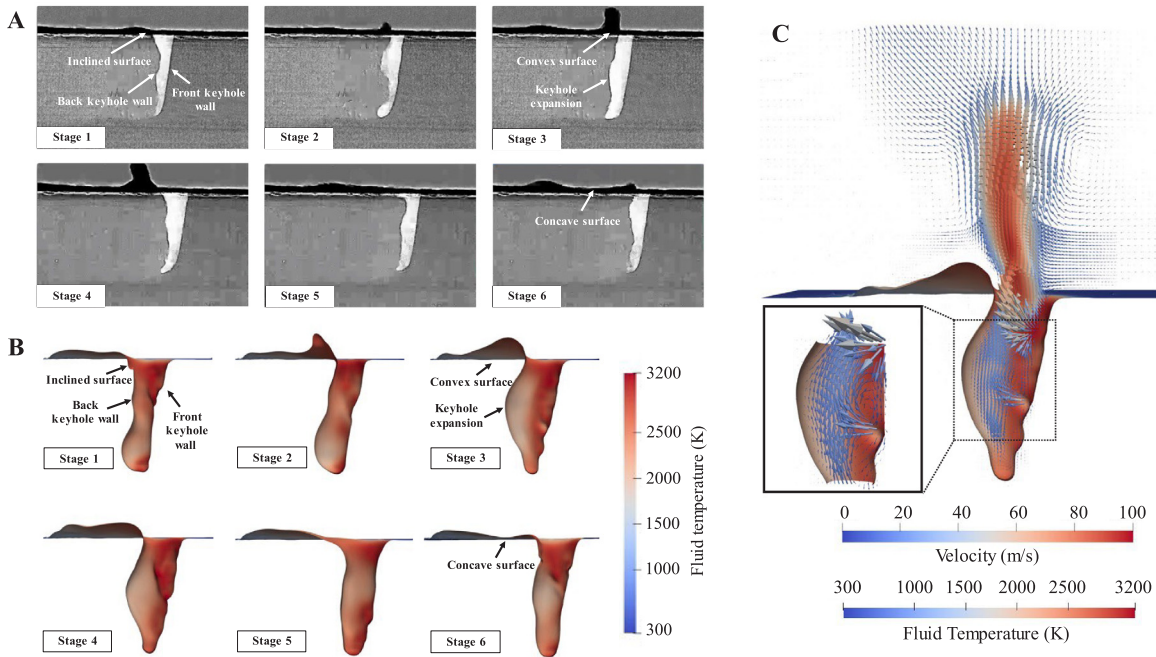


Fig. 12. Comparison of the simulated melt pool evolution with experimental observations where the melt pool develops a representative cycle of six stages according to surface melt pool shape changes which are directly correlate to the keyhole dynamics dictated by the vapor generation and motion at the keyhole wall. (A) Snapshots of melt pool evolution during melting process obtained from the supplementary materials [92]. The laser power is 520 W and the scanning velocity is 70 cm/s (corresponding to Case VIII herein). (B) Half sections of melt pool for case VIII. (C) Contour of velocity vector of vapor (inset shown a magnified view in the keyhole bulge portion) along the center profile of Case VIII.

gravity and surface tension, forming a convex surface as shown in Stage 3 in Fig. 12B. Its continuous flow leads to the observation in Stage 4 to Stage 6 in Fig. 12B. It is particularly interesting to observe the direction causation of a bulging keyhole showing a shrinking throat with the subsequent buildup and collapse of the surface heave flow of the melt pool as shown in Fig. 12C. Such mechanism would not have been possibly revealed without physical consideration of vapor and vapor dynamics in a numerical simulation.

It is interesting to further elaborate the evolving surface melt pool buildup caused by the vapor circulation and periodic depression of keyhole morphology. Evidently from Fig. 12B, the melt pool liquid pushed up onto the surface undergoes an evolving surface morphology in the following typical sequence: (1) an initial relatively flat, forward inclined shape at Stage 1; (2) a buildup of sharp heave due to more liquid being pushed out from the keyhole by the vapor (Stage 2); (3) the backward collapse of the heave to form a lower convex surface (Stage 3); and (4) continuous spread of the surface melt pool to a flat surface (stages 4 to 6). This process is iteratively repeated as a representative evolution cycle for melt pool, confirmed by both our numerical simulations and X-ray imaging [92]. These sequential evolutions are directly related to the morphological and volumetric changes of the keyhole under dynamic impact of high-speed vapor during these stages.

3.7. Powder motion driven by joint force of high-speed vapor and entrained gas vortex

It is frequently observed in experiments that powder particles close to the laser beam are entrained or dispelled to leave the powder bed under the joint influence of high-speed vapor and ambient gas, which may cause scattering and spattering of powders during the laser melting process, as shown by the snapshot shown in Fig. 13A [6]. This may further undermine the quality of built parts. To examine the melting induced powder motion, we present in Fig. 13B, C our simulations on the evolution of melt track, vapor and powder motions during the melting process. It is evident that the high-speed vapors generated from the melt pool can mobilize the surrounding unmolten solid powders to displace and scatter, the direction of which depends crucially on the vapor flow characteristics. Note

that the powder bed in our simulation is composed of only two layers and the top layer is more vulnerable for such mobilization. To inspect the detailed variation of powder motions in response to the vapor flow, we further present in Fig. 13D the contours of velocity vector of vapor flow in four regions of the powder bed at 140 μs of our simulation, where regions I and II, regions III and IV are chosen to the left and right sides of the generated vapor as shown in the figure, respectively. The vapor inclination in this case is backwards, similar to the observed case in Fig. 13A. The particles in the top portion of region I are pushed backwards along the vapor flow direction, with a velocity at around 8 m/s. Similar velocity vector of the entrained ambient gas shown in region IV accounts for the lifting of powders in front of the laser beam. Two mild vortices can be found at the ambient gas–vapor interface in Region II and III, similar to the observation in Fig. 11, where the particles can be mobilized to move at a speed of several meters per second. The vortex in region II will lift the affected powders into the vapor flow and carry them to fall back into the surface melt pool of the solidified surface; the vortex in Region III can pull the moving powders in the ambient gas back into the vapor flow and some of them may further fall into the melt pool. Both mechanisms may possibly help to increase the number of powders melted during the scanning process, but they may also potentially account for some partially molten particles found in the melt pool that contribute to undesired surface roughness and melting quality for the final product. Fig. 13E and F further show detail of the surface characteristics of the vapor flow and melt pool dynamics caused depression, surface melt pool flow, denudation zone, spatters and partially melted powders (c.f. Khairallah et al. [8,49,50]).

4. Discussion

Technological advances on laser powder bed fusion for metal additive manufacturing can be achieved with better understanding of physics and working mechanisms of laser melting process of metallic powders. It mandates the development of new high-fidelity, high-resolution prediction tools to overcome the physical limits of experimental observation techniques [12]. The multi-phase semi-coupled resolved CFD-DEM approach proposed in this study offers such a pathway for future research and development of metallic-powder-based laser melting. The proposed approach has been developed as a general-purpose computational tool to solve a class of multiphase, multiphysics problems for granular solid–fluid systems that involve thermal-induced phase changes (including fusion, vaporization, and solidification) and dynamic interactions among frictional solid grains and multiphase fluids. The method has been applied for simulations of selective laser melting of Ti-6Al-4V powder. The results demonstrate encouraging quantitative and qualitative consistencies with experimental observations and showcase a promising predictive capability. The following discussion is further devoted to several specific aspects pertaining to metallic powder based SLM process, both from numerical modeling and experimental testing technique perspectives, to advance our understanding of SLM to a next level.

First, we highlight in this study the importance of considering vaporization of melt pool liquid and the ensuing vapor flow that impacts essentially all other aspects the laser melting process that need to be modeled. As pointed out by Khairallah et al. [8,49,50], the surface melt pool temperature at the laser spot may reach boiling point to cause vaporization and the generated vapor recoil pressure forces the melt pool surface to create depression. They however have not been able to resolve the vapor flow separation from the liquid phase and further interaction with the ambient gas, which has been rigorously considered in this study. In doing so, five pertinent aspects related to the modeling of physical processes of SLM can be improved. (a) The circulation of high-speed, high-temperature vapors within the depression and their escaping flow to the track surface can contribute equally important as the recoil pressure and Marangoni surface flow do to the morphological variation and instability of keyholes. Indeed, as shown in Fig. 12, the vapor circulated or generated from the bottom part of the keyhole may push an upward movement to escape, during which it changes oscillatorily the backwall profile of the keyhole and causes possible depression instability joining with other forces. Meanwhile, the vapor circulation may contribute partially to the redistribution of temperatures of the keyhole wall and thus possible changes of surface tension and Marangoni surface convection. (b) The mixing process of high-speed vapor escaping from the depression with the surrounding ambient gas can cause interesting vortex flow as shown in Fig. 11 that join forces with the surface Marangoni convection, surface tension, buoyancy, and gravity force to shape the surface melt pool flow and final melt track when cooling down. (c) High-speed vapor may attribute to the sparking and scattering of powder grains as shown in Figs. 9 and 13, in addition to the melt flow induced sparking and spattering [6], to cause possible defects to the final print part [99]. (d) High-speed vapor flow in conjunction with ambient gas vortex may also contribute partially to the so-called “denudation zone” (Fig. 13E, F) coined by Khairallah et al. [8,49,50] that account for the

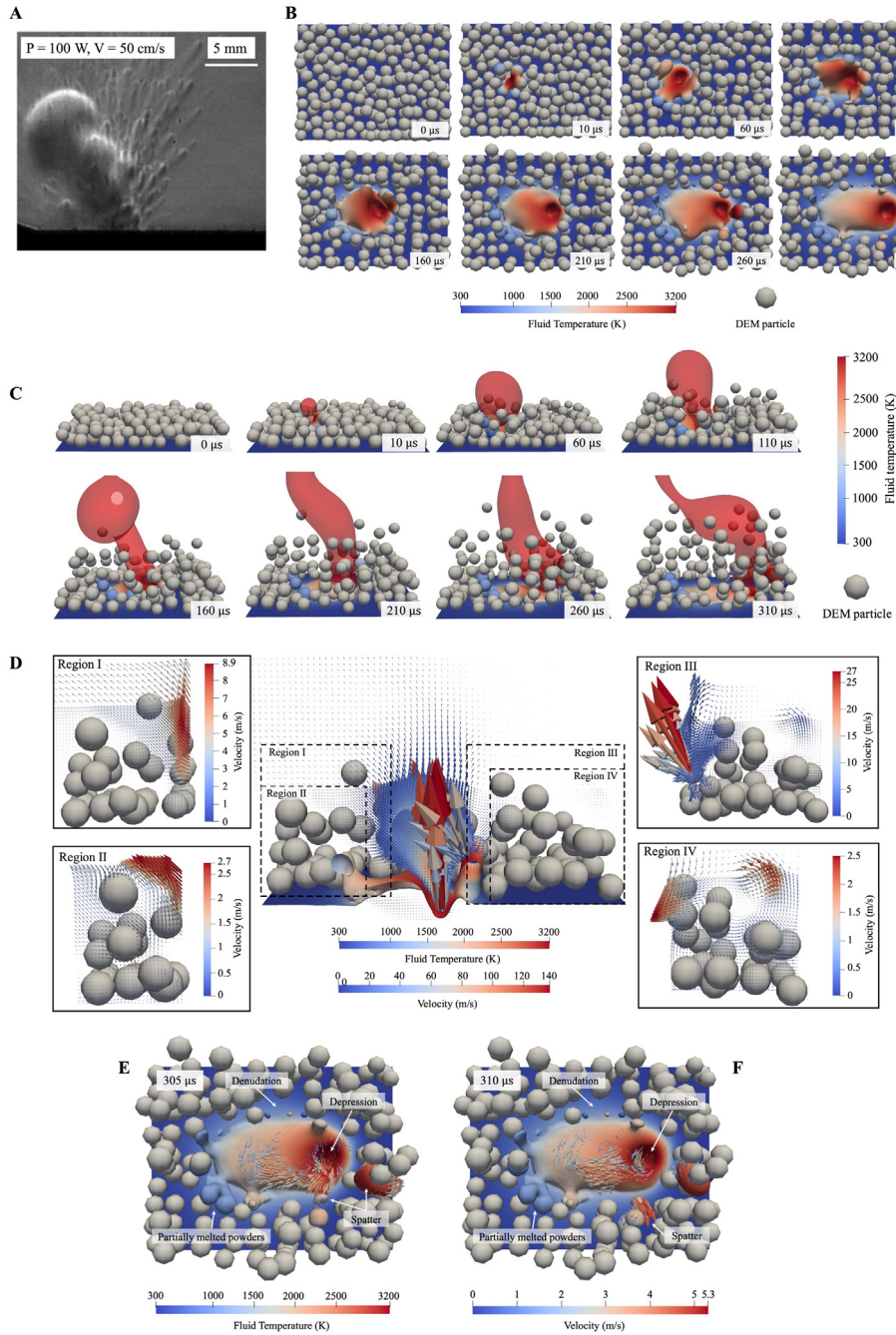


Fig. 13. The experimental result (A) and simulation results (B–D) of powder-based SLM. In this simulation, the laser power is 120 W and the scanning velocity is 700 mm/s. (A) Schlieren images of vapor and entrained powders at 100 W and 500 mm/s [6]. (B) The melt track evolution (top view) during the melting process from 0 μs to 310 μs. (C) The high-speed vapor and vapor-induced powder motions (side view) during the melting process from 0 μs to 310 μs. (D) The half section of melt pool and powders, and the velocity vector contour of the center profile at 140 μs. The drawing of partial enlargement for region I to IV is provided to show clear velocity field. (E & F) Snapshots of refined top view of the melt track at 305 μs and 310 μs, showing key features of the melt pool dynamics including depression, melt pool flow, the denudation zone, spatters, and partially melted powders.

various printing defects such as lateral pores, open and trapped pores as observed experimentally [100–102]. (e) The inclusion of ambient gas flow induced by the metallic vapor flow also helps to offer a possible way to rigorously consider both evaporative and radiative surface cooling of the surface melt pool liquid, so as to determine the surface temperature accurately [8,49,50]. As a result, our integrated coupling framework with full consideration of vaporization and the generated high-speed, high-temperature vapor empowers us to seamlessly combine a full range of forces including recoil pressure, Marangoni convection, surface tension, buoyancy force, laser power absorption by a high-definition ray tracking energy source model, intricate vapor–flow–powder–gas interactions, and their implications on the entire melt pool dynamics [8,49,50]. In recognizing its importance, our study also pinpoints future challenges and directions for experimentalists to develop next-generation observation tools and techniques to capture and quantify the generation of metallic vapors and how complicated physics comes into play during their interactive lifespan with surrounding melt liquid, powders, and ambient gas to shape the entire melting process. High-quality quantifiable experimental data are highly desirable in this respect for future validation of advanced analytical models.

Second, the discrete nature of powders must be properly considered in numerical modeling of SLM. The implication is multifold. (a) Frictional, freely mobilizable powders constitute a key part of the dynamical process of SLM. As shown in Fig. 13, powder motion may be driven by melt pool flow through spattering, by laser generated recoil pressure and the high-speed vapor flow escaping from the keyhole at the top, and by the vortex formed by ambient gas. The inter-particle collision and settling of these mobilized powders may affect the density of surrounding powder layers and possible edge pores for future melting track and can also affect the quality of melt track if they fall into the surface melt pool [98,103]. They may even fall back into the keyhole depression if conditions fit [8], which can cause keyhole instability and generation of possible pores at keyhole tip. Realistic consideration of discrete powders and their motions in different flow fields is critical. The introduction of DEM in our coupling scheme enables the capture of these features flexibly and accurately. (b) High-definition modeling of the partial melting process of each individual powder grain is a critical step in achieving high-fidelity simulation results. As emphasized by Khairallah et al. [8,49,50], the laser rays may land and heat the top of a powder grain to cause inhomogeneous energy deposition and heat diffusion within the powder, which may be further reinforced possible shadowing effect of ray tracks. All these physical processes may cause partial or progressive melting of a powder particle. Our study employs a semi-coupled CFD-DEM in conjunction with a high-resolution ray tracing laser model to resolve the inhomogeneous temperature field within a powder grain to capture the partial or progressive melting realistically. As each DEM particle needs to be matched with a fully resolved CFD mesh to solve the inhomogeneous temperature field for melting in our study, this inevitably incur computational complexity and cost [104]. To improve both efficiency and accuracy or an optimal compromise between the two will be an effort of future research. (c) Powder layer density is an important factor affecting the melting process and melt part quality but has received relatively less attention [84,105,106]. Modeling the layering process of powders as discrete, movable frictional particles can help to achieve this important goal. The use of DEM in our coupling framework lends the convenience to consider this process and to examine the effect of powder layer density on the entire melting process in a rigorous integrated manner.

Third, the availability of such a high-fidelity, high-resolution computational model offers exciting future opportunities to possibly examine key processes of SLM quantitatively for controllable printing design. Amongst many, the most interesting yet challenging aspects of SLM are perhaps the keyhole formation and melt pool dynamics [9,11,92,99]. Their understanding hinges crucially on a quantifiable differentiation of the relevant dominance of influencing forces [9], including the more conventional forces governing most multi-phase flows such as gravity, viscous force, buoyancy, and surface tension, and major thermal related force terms or effects, such as recoil pressure, Marangoni convection and metallic vapor pressure. The stability of keyhole (or depression) is a major concern in laser melting. The stability analysis can indeed be partitioned into two portions of a typical keyhole structure bounded by the keyhole tip, its front wall and the back wall. The characteristics of the front keyhole wall, as shown in Fig. 10, show a uniquely steady tilting angle during the moving of keyhole that is proportional of laser power and scanning velocity. The laser energy is mainly absorbed by the front keyhole wall up to the bottom tip, generating a high temperature (see Figs. 10B and 12C for example) that exceeds the boiling temperature of the melt pool liquid to induce vaporization and causes high recoil pressure in this portion. This recoil pressure acts as a dominant driving force to counterbalance other collapsing forces to maintain the stability of the front wall. The Marangoni's effect is relative secondary since the temperature field of the melt pool liquid in this front wall

side is relatively homogeneous. Nevertheless, the Marangoni convection may help to render a more homogeneous temperature field along the front wall side to enhance the stability. The recoil pressure and Marangoni convection join to counterbalance major collapsing forces including surface tension exerted on the front wall, leading to a dynamically steady front wall for the keyhole. The angle of this wall is dependent on the relative magnitude of the two counterparts, where the recoil pressure can be related to the laser energy density which is further a function of combined laser power and scanning velocity. Future experimental or numerical studies can be devoted to quantitative examination of the threshold of this recoil pressure in relation with the laser energy density and induced vaporization to offer better reference for the design of scanning scheme.

The dynamical oscillation of its back portion of a keyhole during the melting process, as exemplified in Fig. 12A, is in stark contrast to its stable front wall. The oscillation is indeed an integrated portion with the ensuing surface melt pool flow that constitutes the overall melt pool dynamics. The generated vapor and vapor flow in conjunction with recoil pressure play a dominant role in both supporting the keyhole and disrupting its stability at the backwall of the keyhole due to its highly dynamic nature. As shown in Figs. 11C and 12C, the vaporization generates high vapor which may be directed straight toward the back wall or travel downwards, forming a complicated vapor circulation within the keyhole from its bottom and moving further upwards to the top before escaping at different direction to the ambient gas. The entire circulation is highly dynamically and frequently instable, contributing to the observed oscillation of the backwall of the keyhole wherein the vapor pressure counters other forces such as gravity and surface tension. The surface drag force caused by the vapor flow at the top of the sharp bump surface can reach triple Marangoni's flow, as shown in Fig. 11E. Meanwhile, the backwall of keyhole does not possess a temperature as high as the front wall, but the temperature exhibits an apparent decrease from the keyhole tip to the back wall (see Fig. 11B). The temperature gradient along the backwall of the keyhole causes considerable Marangoni's convection which becomes a dominant force along the backwall of the keyhole, and the surface drag force caused by the vapor flow only accounts for around 25% and 5% of the Marangoni's force in the back part of the melt pool (see Fig. 11E). This Marangoni's effect joins hand with the recoil pressure to drive the melt pool liquid to flow from the tip part upwards to the surface. When reaching the surface, the transported melt pool liquid is further forced by the escaping vapor and entrained ambient gas to move backwards, exhibiting different surface flow dynamics as shown in Fig. 12C. During the surface flow process, recoil force, gravity and surface tension also join the force to play a role. The above only provides a qualitative explanation of the observation on keyhole stability and the overall melt pool dynamics. The entire process is complicated and may incur intricate mechanisms for pore defect generation at both the tip and edges of the keyhole [12,107], which demands further refined simulations to quantify the underlying physics in the future.

5. Conclusions

In conclusion, the study offers a next-generation three-dimensional computational tool, based on rigorous coupling of CFD and DEM, that empowers us to investigate rigorously and comprehensively the multiphase, multiphysics mechanisms underlying thermal-induced phase changes in a granular media-fluids system. Its predictive capability is demonstrated by simulations of selective laser melting of Ti-6Al-4V powder and shows a great potential for future quantitative analysis of laser powder bed fusion in metallic additive manufacturing. Specifically, the effect of the high-speed vapor on the melt pool, keyhole, and powders has been discussed in detail. The corresponding mechanism requires further quantitative analysis for improving the SLM technology. As a general-purpose tool, the proposed framework is equally applicable for addressing engineering challenges beyond 3D printing. Tangible problems of important engineering significance that can be tackled by the proposed framework include methane hydrate exploitation [108], soil freeze and thaw in permafrost regions [109], snow avalanches [110], and glacial ice melting [111]. Methodologically, the high computational cost incurred by the multiphase, multiway coupling magnified by fine temporal and spatial resolutions may pose a major drawback restricting its practical applications for large-scale simulations, the solution of which mandates efficient parallel computing techniques on high-performance computing facilities. Note that all cases included in this study have been run on the Tianhe II National Supercomputer. In addition, highly refined simulations are required to gain deeper insights into the microscopic dynamics of keyhole and melt pool, such as the porosity generation mechanism at the moving keyhole tip and the dynamics of the generated inner pores in the melt pool. Finally, the proposed numerical framework needs substantial further extension to enable seamless, systematic investigation of the mechanical behavior of the built parts, such as the surface roughness, porosity, and mechanical properties. The extension may be built upon further enrichments of our multi-layer DEM model [53] or coupling with other numerical methods such as FEM as a mechanical solver, which will be explored in the future.

Declaration of competing interest

The authors declare that they have no known competing financial interests or personal relationships that could have appeared to influence the work reported in this paper.

Data availability

Data will be made available on request.

Acknowledgments

The study was financially supported by National Natural Science Foundation of China (via General Project #11972030) and Research Grants Council of Hong Kong (under GRF #16205418). Part of this work was financially supported by the Project of Hetao Shenzhen-Hong Kong Science and Technology Innovation Cooperation Zone (HZQB-KCZYB-2020083). T.Y. acknowledges the sponsorship of Hong Kong Ph.D. Fellowship from Research Grants Council of Hong Kong for his Ph.D. study. The authors also wish to thank all three anonymous reviewers for their constructive comments on the manuscript.

References

- [1] T. DebRoy, H. Wei, J. Zuback, T. Mukherjee, J. Elmer, J. Milewski, A.M. Beese, A.d. Wilson-Heid, A. De, W. Zhang, Additive manufacturing of metallic components—process, structure and properties, *Prog. Mater. Sci.* 92 (2018) 112–224.
- [2] D.L. Bourell, M.C. Leu, D.W. Rosen, Roadmap for Additive Manufacturing: Identifying the Future of Freeform Processing, The University of Texas at Austin, Austin, TX, 2009, pp. 11–15.
- [3] S. Srivatsa, Additive Manufacturing (AM) Design and Simulation Tools Study, Final Report, Air Force Research Laboratory, 2014, WP AFB OH.
- [4] T. Zohdi, N. Castrillon, Variability of targeted material thermal responses to laser-induced heating in additive manufacturing, *J. Manuf. Sci. Eng.* 141 (2019) 081012.
- [5] S. Ly, A.M. Rubenchik, S.A. Khairallah, G. Guss, M.J. Matthews, Metal vapor micro-jet controls material redistribution in laser powder bed fusion additive manufacturing, *Sci. Rep.* 7 (2017) 1–12.
- [6] P. Bidare, I. Bitharas, R. Ward, M. Attallah, A.J. Moore, Fluid and particle dynamics in laser powder bed fusion, *Acta Mater.* 142 (2018) 107–120.
- [7] G. Strano, L. Hao, R.M. Everson, K.E. Evans, Surface roughness analysis, modelling and prediction in selective laser melting, *J. Mater. Process. Technol.* 213 (2013) 589–597.
- [8] S.A. Khairallah, A.T. Anderson, A. Rubenchik, W.E. King, Laser powder-bed fusion additive manufacturing: Physics of complex melt flow and formation mechanisms of pores, spatter, and denudation zones, *Acta Mater.* 108 (2016) 36–45.
- [9] S.M.H. Hojjatzadeh, N.D. Parab, W. Yan, Q. Guo, L. Xiong, C. Zhao, M. Qu, L.I. Escano, X. Xiao, K. Fezzaa, Pore elimination mechanisms during 3D printing of metals, *Nature Commun.* 10 (2019) 1–8.
- [10] R. Cunningham, A. Nicolas, J. Madsen, E. Fodran, E. Anagnostou, M.D. Sangid, A.D. Rollett, Analyzing the effects of powder and post-processing on porosity and properties of electron beam melted Ti-6Al-4V, *Mater. Res. Lett.* 5 (2017) 516–525.
- [11] C. Zhao, N.D. Parab, X. Li, K. Fezzaa, W. Tan, A.D. Rollett, T. Sun, Critical instability at moving keyhole tip generates porosity in laser melting, *Science* 370 (2020) 1080–1086.
- [12] S.A. Khairallah, A.A. Martin, J.R. Lee, G. Guss, N.P. Calta, J.A. Hammons, M.H. Nielsen, K. Chaput, E. Schwalbach, M.N. Shah, Controlling interdependent meso-nanosecond dynamics and defect generation in metal 3D printing, *Science* 368 (2020) 660–665.
- [13] H. Chen, W. Yan, Spattering and denudation in laser powder bed fusion process: Multiphase flow modelling, *Acta Mater.* 196 (2020) 154–167.
- [14] T. Sun, Probing ultrafast dynamics in laser powder bed fusion using high-speed X-ray imaging: A review of research at the advanced photon source, *JOM* 72 (2020) 999–1008.
- [15] R. Ganeriwala, T.I. Zohdi, A coupled discrete element-finite difference model of selective laser sintering, *Granul. Matter* 18 (2016) 21.
- [16] A. Otto, H. Koch, R.G. Vazquez, Multiphysical simulation of laser material processing, *Physics Procedia* 39 (2012) 843–852.
- [17] F.J. Gürtler, M. Karg, K.H. Leitz, M. Schmidt, Simulation of laser beam melting of steel powders using the three-dimensional volume of fluid method, *Physics Procedia* 41 (2013) 881–886.
- [18] A. Otto, H. Koch, K.-H. Leitz, M. Schmidt, Numerical simulations - a versatile approach for better understanding dynamics in laser material processing, *Physics Procedia* 12 (2011) 11–20.
- [19] A. Otto, M. Schmidt, Towards a universal numerical simulation model for laser material processing, *Physics Procedia* 5 (2010) 35–46.
- [20] Z. Wang, W. Yan, W.K. Liu, M. Liu, Powder-scale multi-physics modeling of multi-layer multi-track selective laser melting with sharp interface capturing method, *Comput. Mech.* 63 (2018) 649–661.
- [21] J. Tan, C. Tang, C. Wong, Study and modeling of melt pool evolution in selective laser melting process of SS316L, *MRS Commun.* 8 (2018) 1178–1183.
- [22] H. Mindt, O. Desmaison, M. Megahed, Modelling powder bed additive manufacturing defects, 2015.

- [23] H.-W. Mindt, O. Desmaison, M. Megahed, A. Peralta, J. Neumann, Modeling of powder bed manufacturing defects, *J. Mater. Eng. Perform.* 27 (2018) 32–43.
- [24] H. Mindt, M. Megahed, N. Lavery, M. Holmes, S. Brown, Powder bed layer characteristics: the overseen first-order process input, *Metall. Mater. Trans. A* 47 (2016) 3811–3822.
- [25] N. N'Dri, H.-W. Mindt, B. Shula, M. Megahed, A. Peralta, P. Kantzos, J. Neumann, TMS 2015 144th Annual Meeting & Exhibition, Springer, 2015.
- [26] A. Peralta, M. Enright, M. Megahed, J. Gong, M. Roybal, J. Craig, Towards rapid qualification of powder-bed laser additively manufactured parts, *Integr. Mater. Manuf. Innov.* 5 (2016) 154–176.
- [27] J. Zielinski, S. Vervoort, H.-W. Mindt, M. Megahed, Influence of powder bed characteristics on material quality in additive manufacturing, *BHM Berg- Huettenmaenn. Mon.hefte* 162 (2017) 192–198.
- [28] J. Zielinski, H.-W. Mindt, J. Düchting, J.H. Schleifenbaum, M. Megahed, Numerical and experimental study of Ti6Al4V components manufactured using powder bed fusion additive manufacturing, *JOM* 69 (2017) 2711–2718.
- [29] M. Markl, C. Körner, Multiscale modeling of powder bed-based additive manufacturing, *Annu. Rev. Mater. Res.* 46 (2016) 93–123.
- [30] A. Klassen, T. Scharowsky, C. Körner, Evaporation model for beam based additive manufacturing using free surface lattice Boltzmann methods, *J. Phys. D: Appl. Phys.* 47 (2014).
- [31] A. Klassen, V.E. Forster, C. Körner, A multi-component evaporation model for beam melting processes, *Modelling Simulation Mater. Sci. Eng.* 25 (2017).
- [32] A. Klassen, A. Bauereiz, C. Körner, Modelling of electron beam absorption in complex geometries, *J. Phys. D: Appl. Phys.* 47 (2014).
- [33] R. Ammer, M. Markl, U. Ljungblad, C. Körner, U. Rüde, Simulating fast electron beam melting with a parallel thermal free surface lattice Boltzmann method, *Comput. Math. Appl.* 67 (2014) 318–330.
- [34] A. Klassen, V.E. Forster, V. Juechter, C. Körner, Numerical simulation of multi-component evaporation during selective electron beam melting of tial, *J. Mater. Process. Technol.* 247 (2017) 280–288.
- [35] C. Körner, A. Bauereiz, E. Attar, Fundamental consolidation mechanisms during selective beam melting of powders, *Modelling Simulation Mater. Sci. Eng.* 21 (2013).
- [36] R. Ammer, U. Rüde, M. Markl, V. Jüchter, C. Körner, Validation experiments for LBM simulations of electron beam melting, *Internat. J. Modern Phys. C* 25 (2014).
- [37] A.M. Rausch, V.E. Küng, C. Pobel, M. Markl, C. Körner, Predictive simulation of process windows for powder bed fusion additive manufacturing: Influence of the powder bulk density, *Materials* 10 (2017).
- [38] E. Attar, C. Körner, Lattice Boltzmann model for thermal free surface flows with liquid–solid phase transition, *Int. J. Heat Fluid Flow* 32 (2011) 156–163.
- [39] D. Riedlbauer, T. Scharowsky, R.F. Singer, P. Steinmann, C. Körner, J. Mergheim, Macroscopic simulation and experimental measurement of melt pool characteristics in selective electron beam melting of Ti-6Al-4V, *Int. J. Adv. Manuf. Technol.* 88 (2017) 1309–1317.
- [40] A. Rai, H. Helmer, C. Körner, Simulation of grain structure evolution during powder bed based additive manufacturing, *Addit. Manuf.* 13 (2017) 124–134.
- [41] A. Rai, M. Markl, C. Körner, A coupled cellular automaton–lattice Boltzmann model for grain structure simulation during additive manufacturing, *Comput. Mater. Sci.* 124 (2016) 37–48.
- [42] T.I. Zohdi, Rapid simulation of laser processing of discrete particulate materials, *Arch. Comput. Methods Eng.* 20 (2013) 309–325.
- [43] T.I. Zohdi, Additive particle deposition and selective laser processing—a computational manufacturing framework, *Comput. Mech.* 54 (2014) 171–191.
- [44] T. Zohdi, On the thermal response of a laser-irradiated powder particle in additive manufacturing, *CIRP J. Manuf. Sci. Technol.* 10 (2015) 7783.
- [45] T. Zohdi, Modeling and simulation of laser processing of particulate-functionalized materials, *Arch. Comput. Methods Eng.* 24 (2017) 89–113.
- [46] T. Zohdi, Construction of a rapid simulation design tool for thermal responses to laser-induced feature patterns, *Comput. Mech.* 62 (2018) 393–409.
- [47] T. Zohdi, Ultra-fast laser-patterning computation for advanced manufacturing of powdered materials exploiting knowledge-based heat-kernels, *Comput. Methods Appl. Mech. Engrg.* 343 (2019) 234–248.
- [48] T. Maeshima, Y. Kim, T.I. Zohdi, Particle-scale numerical modeling of thermo-mechanical phenomena for additive manufacturing using the material point method, *Comput. Part. Mech.* 8 (2021) 613–623.
- [49] Y. Yang, O. Ragnvaldsen, Y. Bai, M. Yi, B.-X. Xu, 3D non-isothermal phase-field simulation of microstructure evolution during selective laser sintering, *Npj Comput. Mater.* 5 (2019) 1–12.
- [50] A.J. Pinkerton, An analytical model of beam attenuation and powder heating during coaxial laser direct metal deposition, *J. Phys. D: Appl. Phys.* 40 (2007) 7323.
- [51] M. Bayat, A. Thanki, S. Mohanty, A. Witvrouw, S. Yang, J. Thorborg, N.S. Tiedje, J.H. Hattel, Keyhole-induced porosities in laser-based powder bed fusion (L-PBF) of Ti6Al4V: High-fidelity modelling and experimental validation, *Addit. Manuf.* 30 (2019) 100835.
- [52] X. Li, C. Zhao, T. Sun, W. Tan, Revealing transient powder-gas interaction in laser powder bed fusion process through multi-physics modeling and high-speed synchrotron x-ray imaging, *Addit. Manuf.* 35 (2020) 101362.
- [53] T. Yu, J. Zhao, Semi-coupled resolved CFD–DEM simulation of powder-based selective laser melting for additive manufacturing, *Comput. Methods Appl. Mech. Engrg.* 377 (2021) 113707.

- [54] J.-H. Cho, S.-J. Na, Implementation of real-time multiple reflection and fresnel absorption of laser beam in keyhole, *J. Phys. D: Appl. Phys.* 39 (2006) 5372.
- [55] W. Tan, N.S. Bailey, Y.C. Shin, Investigation of keyhole plume and molten pool based on a three-dimensional dynamic model with sharp interface formulation, *J. Phys. D: Appl. Phys.* 46 (2013) 055501.
- [56] Y. Liu, Y. Yang, S. Mai, D. Wang, C. Song, Investigation into spatter behavior during selective laser melting of AISI 316L stainless steel powder, *Mater. Des.* 87 (2015) 797–806.
- [57] V.R. Voller, M. Cross, N. Markatos, An enthalpy method for convection/diffusion phase change, *Internat. J. Numer. Methods Engrg.* 24 (1987) 271–284.
- [58] F. Rösler, D. Brüggemann, Shell-and-tube type latent heat thermal energy storage: numerical analysis and comparison with experiments, *Heat Mass Transf.* 47 (2011) 1027–1033.
- [59] J. Roenby, H. Bredmose, H. Jasak, A computational method for sharp interface advection, *R. Soc. Open Sci.* 3 (2016) 160405.
- [60] M. Rudman, Volume-tracking methods for interfacial flow calculations, *Internat. J. Numer. Methods Fluids* 24 (1997) 671–691.
- [61] C.J. Greenshields, *OpenFOAM User Guide*, OpenFOAM Foundation Ltd, 2015, p. 47, version 3.
- [62] M. Rudman, A volume-tracking method for incompressible multifluid flows with large density variations, *Internat. J. Numer. Methods Fluids* 28 (1998) 357–378.
- [63] J. Roenby, H. Bredmose, H. Jasak, *OpenFOAM®*, Springer, 2019.
- [64] H. Wessels, C. Weizenfels, P. Wriggers, Metal particle fusion analysis for additive manufacturing using the stabilized optimal transportation meshfree method, *Comput. Methods Appl. Mech. Engrg.* 339 (2018) 91–114.
- [65] L. Wang, Y. Zhang, W. Yan, Evaporation model for keyhole dynamics during additive manufacturing of metal, *Phys. Rev. A* 14 (2020) 064039.
- [66] A.V. Gusarov, I. Smurov, Gas-dynamic boundary conditions of evaporation and condensation: numerical analysis of the Knudsen layer, *Phys. Fluids* 14 (2002) 4242–4255.
- [67] K. Aoki, C. Bardos, S. Takata, Knudsen layer for gas mixtures, *J. Stat. Phys.* 112 (2003) 629–655.
- [68] S. Verma, A. Dewan, Assessment of characteristics of Phase Change Region during solidification of a binary alloy in different flow regimes, *Mater. Today: Proc.* 4 (2017) 9445–9449.
- [69] C. Panwisawas, C. Qiu, M.J. Anderson, Y. Sovani, R.P. Turner, M.M. Attallah, J.W. Brooks, H.C. Basoalto, Mesoscale modelling of selective laser melting: thermal fluid dynamics and microstructural evolution, *Comput. Mater. Sci.* 126 (2017) 479–490.
- [70] J.L. Tan, C. Tang, C.H. Wong, Study and modeling of melt pool evolution in selective laser melting process of SS316L, *MRS Commun.* 8 (2018) 1178–1183.
- [71] Z. Wang, W. Yan, W.K. Liu, M. Liu, Powder-scale multi-physics modeling of multi-layer multi-track selective laser melting with sharp interface capturing method, *Comput. Mech.* 63 (2019) 649–661.
- [72] Z.S. Saldi, Marangoni driven free surface flows in liquid weld pools, 2012.
- [73] J.U. Brackbill, D.B. Kothe, C. Zemach, A continuum method for modeling surface tension, *J. Comput. Phys.* 100 (1992) 335–354.
- [74] J. Ahn, S.-J. Na, Three-dimensional thermal simulation of nanosecond laser ablation for semitransparent material, *Appl. Surf. Sci.* 283 (2013) 115–127.
- [75] T. Mukherjee, J. Zuback, A. De, T. DebRoy, 7th International Symposium on High-Temperature Metallurgical Processing, Springer, 2016.
- [76] M. Gharbi, P. Peyre, C. Gorny, M. Carin, S. Morville, P. Le Masson, D. Carron, R. Fabbro, Influence of various process conditions on surface finishes induced by the direct metal deposition laser technique on a Ti–6Al–4V alloy, *J. Mater. Process. Technol.* 213 (2013) 791–800.
- [77] R. McVey, R. Melnychuk, J. Todd, R. Martukanitz, Absorption of laser irradiation in a porous powder layer, *J. Laser Appl.* 19 (2007) 214–224.
- [78] A.A. Shirgaonkar, M.A. MacIver, N.A. Patankar, A new mathematical formulation and fast algorithm for fully resolved simulation of self-propulsion, *J. Comput. Phys.* 228 (2009) 2366–2390.
- [79] A. Di Renzo, F.P. Di Maio, Comparison of contact-force models for the simulation of collisions in DEM-based granular flow codes, *Chem. Eng. Sci.* 59 (2004) 525–541.
- [80] A.B. Stevens, C. Hrenya, Comparison of soft-sphere models to measurements of collision properties during normal impacts, *Powder Technol.* 154 (2005) 99–109.
- [81] H. Zhu, Z. Zhou, R. Yang, A. Yu, Discrete particle simulation of particulate systems: theoretical developments, *Chem. Eng. Sci.* 62 (2007) 3378–3396.
- [82] A. Bérard, G.S. Patience, B. Blais, Experimental methods in chemical engineering: Unresolved CFD-DEM, *Can. J. Chem. Eng.* 98 (2020) 424–440.
- [83] C. Panwisawas, Y. Sovani, R.P. Turner, J.W. Brooks, H.C. Basoalto, I. Choquet, Modelling of thermal fluid dynamics for fusion welding, *J. Mater. Process. Technol.* 252 (2018) 176–182.
- [84] C. Qiu, C. Panwisawas, M. Ward, H.C. Basoalto, J.W. Brooks, M.M. Attallah, On the role of melt flow into the surface structure and porosity development during selective laser melting, *Acta Mater.* 96 (2015) 72–79.
- [85] C. Goniva, C. Kloss, N.G. Deen, J.A. Kuipers, S. Pirker, Influence of rolling friction on single spout fluidized bed simulation, *Particuology* 10 (2012) 582–591.
- [86] C. Kloss, C. Goniva, A. Hager, S. Amberger, S. Pirker, Models, algorithms and validation for opensource DEM and CFD-DEM, *Prog. Comput. Fluid Dyn. Int. J.* 12 (2012) 140–152.
- [87] R.I. Issa, Solution of the implicitly discretised fluid flow equations by operator-splitting, *J. Comput. Phys.* 62 (1986) 40–65.
- [88] V. Vuorinen, J.-P. Keskinen, C. Duwig, B. Boersma, On the implementation of low-dissipative Runge–Kutta projection methods for time dependent flows using OpenFOAM®, *Comput. & Fluids* 93 (2014) 153–163.

- [89] B. Blais, M. Lassaigne, C. Goniva, L. Fradette, F. Bertrand, A semi-implicit immersed boundary method and its application to viscous mixing, *Comput. Chem. Eng.* 85 (2016) 136–146.
- [90] A. Hager, *Cfd-Dem on Multiple Scales-an Extensive Investigation of Particle-Fluid Interactions*, Johannes Kepler University Linz, Linz, 2014.
- [91] Z. Zhou, S. Kuang, K. Chu, A. Yu, Discrete particle simulation of particle–fluid flow: model formulations and their applicability, *J. Fluid Mech.* 661 (2010) 482–510.
- [92] R. Cunningham, C. Zhao, N. Parab, C. Kantzos, J. Pauza, K. Fezzaa, T. Sun, A.D. Rollett, Keyhole threshold and morphology in laser melting revealed by ultrahigh-speed x-ray imaging, *Science* 363 (2019) 849–852.
- [93] S. Lu, W. Dong, D. Li, Y. Li, Numerical study and comparisons of gas tungsten arc properties between argon and nitrogen, *Comput. Mater. Sci.* 45 (2009) 327–335.
- [94] A. Masmoudi, R. Bolot, C. Coddet, Investigation of the laser–powder–atmosphere interaction zone during the selective laser melting process, *J. Mater. Process. Technol.* 225 (2015) 122–132.
- [95] P.J. Linstrom, NIST chemistry webbook, 2005, <http://webbook.nist.gov>.
- [96] M. Ghatee, M. Sanchooli, Viscosity and thermal conductivity of cesium vapor at high temperatures, *Fluid Phase Equilib.* 214 (2003) 197–209.
- [97] A.Y. Polishchuk, É. Shpil’Rain, I. Yakubov, Thermal conductivity and viscosity of lithium vapors, *J. Eng. Phys.* 38 (1980) 247–250.
- [98] M.J. Matthews, G. Guss, S.A. Khairallah, A.M. Rubenchik, P.J. Depond, W.E. King, Denudation of metal powder layers in laser powder bed fusion processes, *Acta Mater.* 114 (2016) 33–42.
- [99] A.A. Martin, N.P. Calta, S.A. Khairallah, J. Wang, P.J. Depond, A.Y. Fong, V. Thampy, G.M. Guss, A.M. Kiss, K.H. Stone, Dynamics of pore formation during laser powder bed fusion additive manufacturing, *Nature Commun.* 10 (2019) 1–10.
- [100] L. Thijs, F. Verhaeghe, T. Craeghs, J. Van Humbeeck, J.-P. Kruth, A study of the microstructural evolution during selective laser melting of Ti–6Al–4V, *Acta Mater.* 58 (2010) 3303–3312.
- [101] L. Thijs, K. Kempen, J.-P. Kruth, J. Van Humbeeck, Fine-structured aluminium products with controllable texture by selective laser melting of pre-alloyed AlSi10Mg powder, *Acta Mater.* 61 (2013) 1809–1819.
- [102] C. Qiu, N.J. Adkins, M.M. Attallah, Microstructure and tensile properties of selectively laser-melted and of HIPed laser-melted Ti–6Al–4V, *Mater. Sci. Eng. A* 578 (2013) 230–239.
- [103] Q. Guo, C. Zhao, L.I. Escano, Z. Young, L. Xiong, K. Fezzaa, W. Everhart, B. Brown, T. Sun, L. Chen, Transient dynamics of powder spattering in laser powder bed fusion additive manufacturing process revealed by in-situ high-speed high-energy x-ray imaging, *Acta Mater.* 151 (2018) 169–180.
- [104] A. Hager, C. Kloss, S. Pirker, C. Goniva, Parallel resolved open source CFD-DEM: method, validation and application, *J. Comput. Multiph. Flows* 6 (2014) 13–27.
- [105] R. Li, J. Liu, Y. Shi, L. Wang, W. Jiang, Balling behavior of stainless steel and nickel powder during selective laser melting process, *Int. J. Adv. Manuf. Technol.* 59 (2012) 1025–1035.
- [106] A.B. Spierings, N. Herres, G. Levy, Influence of the particle size distribution on surface quality and mechanical properties in AM steel parts, *Rapid Prototyp. J.* (2011).
- [107] N. Contuzzi, S. Campanelli, A. Ludovico, 3 d finite element analysis in the selective laser melting process, *Int. J. Simul. Modell.* 10 (2011) 113–121.
- [108] T.-T. Nguyen, D. Waldmann, T.Q. Bui, Computational chemo-thermo-mechanical coupling phase-field model for complex fracture induced by early-age shrinkage and hydration heat in cement-based materials, *Comput. Methods Appl. Mech. Engrg.* 348 (2019) 1–28.
- [109] S. Na, W. Sun, Computational thermo-hydro-mechanics for multiphase freezing and thawing porous media in the finite deformation range, *Comput. Methods Appl. Mech. Engrg.* 318 (2017) 667–700.
- [110] J. Gaume, T. Gast, J. Teran, A. Van Herwijnen, C. Jiang, Dynamic anticrack propagation in snow, *Nature Commun.* 9 (2018) 1–10.
- [111] S. Kang, T. Bui-Thanh, T. Arbogast, A hybridized discontinuous Galerkin method for a linear degenerate elliptic equation arising from two-phase mixtures, *Comput. Methods Appl. Mech. Engrg.* 350 (2019) 315–336.